



An ALMA Spectroscopic Survey of the Brightest Submillimeter Galaxies in the SCUBA-2-COSMOS Field (AS2COSPEC): Survey Description and First Results

Chian-Chou Chen (陳建州)¹ , Cheng-Lin Liao^{1,2}, Ian Smail³ , A. M. Swinbank³ , Y. Ao⁴ , A. J. Bunker⁵, S. C. Chapman^{6,7,8}, B. Hatsukade⁹ , R. J. Ivison¹⁰ , Minju M. Lee^{11,12,13} , Stephen Serjeant¹⁴ , Hideki Umehata^{15,16} , Wei-Hao Wang¹ , and Y. Zhao¹⁷

¹ Academia Sinica Institute of Astronomy and Astrophysics (ASIAA), No. 1, Sec. 4, Roosevelt Road, Taipei 10617, Taiwan; ccchen@asiaa.sinica.edu.tw

² Graduate Institute of Astrophysics, National Taiwan University, Taipei 10617, Taiwan

³ Centre for Extragalactic Astronomy, Department of Physics, Durham University, South Road, Durham DH1 3LE, UK

⁴ Purple Mountain Observatory and Key Laboratory for Radio Astronomy, Chinese Academy of Sciences, Nanjing, People's Republic of China

⁵ Department of Physics, University of Oxford, Keble Road, Oxford OX13RH, UK

⁶ Department of Physics and Astronomy, University of British Columbia, 6225 Agricultural Road, Vancouver V6T 1Z1, Canada

⁷ National Research Council, Herzberg Astronomy and Astrophysics, 5071 West Saanich Road, Victoria V9E 2E7, Canada

⁸ Eureka Scientific, Inc., 2452 Delmer Street Suite 100, Oakland, CA 94602-3017, USA

⁹ Institute of Astronomy, Graduate School of Science, The University of Tokyo, 2-21-1 Osawa, Mitaka, Tokyo 181-0015, Japan

¹⁰ European Southern Observatory, Karl Schwarzschild Strasse 2, D-85748 Garching, Germany

¹¹ Cosmic Dawn Center (DAWN), Jagtvej 128, DK-2200 Copenhagen N, Denmark

¹² DTU-Space, Technical University of Denmark, Elektrovej 327, DK-2800 Kgs. Lyngby, Denmark

¹³ Max-Planck-Institut für Extraterrestrische Physik (MPE), Giessenbachstr. 1, D-85748 Garching, Germany

¹⁴ School of Physical Sciences, The Open University, Milton Keynes, MK7 6AA, UK

¹⁵ Institute for Cosmic Ray Research, The University of Tokyo, 5-1-5 Kashiwanoha, Kashiwa, Chiba 277-8582, Japan

¹⁶ Institute of Astronomy, The University of Tokyo, 2-21-1 Osawa, Mitaka, Tokyo 181-0015, Japan

¹⁷ Yunnan Observatories, Chinese Academy of Sciences, Guandu District, Kunming 650011, People's Republic of China

Received 2021 December 8; revised 2022 March 18; accepted 2022 March 27; published 2022 April 25

Abstract

We introduce an ALMA band 3 spectroscopic survey targeting the brightest submillimeter galaxies (SMGs) in the COSMOS field. Here we present the first results based on the 18 primary SMGs that have $870\ \mu\text{m}$ flux densities of $S_{870} = 12.4\text{--}19.3\ \text{mJy}$ and are drawn from a parent sample of 260 ALMA-detected SMGs from the AS2COSMOS survey. We detect emission lines in 17 and determine their redshifts to be in the range of $z = 2\text{--}5$ with a median of 3.3 ± 0.3 . We confirm that SMGs with brighter S_{870} are located at higher redshifts. The data additionally cover five fainter companion SMGs, and we obtain line detection in one. Together with previous studies, our results indicate that for SMGs that satisfy our selection, their brightest companion SMGs are physically associated with their corresponding primary SMGs $\geq 40\%$ of the time, suggesting that mergers play a role in the triggering of star formation. By modeling the foreground gravitational fields, $< 10\%$ of the primary SMGs can be strongly lensed with a magnification $\mu > 2$. We determine that about 90% of the primary SMGs have lines that are better described by double Gaussian profiles, and the median separation of the two Gaussian peaks is $430 \pm 40\ \text{km s}^{-1}$. This allows estimates of an average baryon mass, which, together with the line dispersion measurements, puts our primary SMGs on the similar mass- σ correlation found on local early-type galaxies. Finally, the number density of our $z > 4$ primary SMGs is found to be $1_{-0.6}^{+0.9} \times 10^{-6}\ \text{cMpc}^{-3}$, suggesting that they can be the progenitors of $z \sim 3\text{--}4$ massive quiescent galaxies.

Unified Astronomy Thesaurus concepts: [Galaxy evolution \(594\)](#); [Galaxy formation \(595\)](#); [High-redshift galaxies \(734\)](#); [Galaxy distances \(590\)](#); [Galaxy counts \(588\)](#); [Interstellar line emission \(844\)](#); [Submillimeter astronomy \(1647\)](#); [Strong gravitational lensing \(1643\)](#)

1. Introduction

Galaxies that are bright in the far-infrared and submillimeter host sites of both vigorous star formation and active black hole growth (Sanders et al. 1988). Predominantly at $z = 1\text{--}4$ (e.g., Chapman et al. 2005; Ivison et al. 2007; Wardlow et al. 2011; Casey et al. 2014; Hodge & da Cunha 2020), recent studies focusing on submillimeter galaxies (SMGs) that are bright at $850\ \mu\text{m}$ ($S_{850} \gtrsim 1\ \text{mJy}$) found that they are some of the most massive systems during these epochs, sitting at the massive end of the stellar mass functions (Dye et al. 2008; Hainline et al. 2011; Michałowski et al. 2012; Koprowski et al. 2016;

Dudzevičiūtė et al. 2020), molecular gas mass functions (Bothwell et al. 2013; Birkin et al. 2021), dust mass functions (da Cunha et al. 2015, 2021), and halo mass functions (Hickox et al. 2012; Chen et al. 2016; Wilkinson et al. 2017; An et al. 2019; Stach et al. 2021). The large cold molecular gas reservoir ($\sim 10^{11}\ M_{\odot}$) estimated from their molecular line measurements is believed to provide the gas supply over ~ 100 Myr timescales for their extensive star formation rates (SFRs) of $\sim 100\text{--}1000\ M_{\odot}\ \text{yr}^{-1}$, similar to the levels of star formation seen in nearby hyper/ultraluminous infrared galaxies (HyLIRGs/ULIRGs; Sanders & Mirabel 1996). Supported by observational evidence including large-scale clustering, the current hypothesis is that SMGs are intimately linked to luminous quasars at similar redshifts and likely followed by phases of compact quiescent galaxies and local massive ellipticals (Lilly et al. 1999; Swinbank et al. 2006;

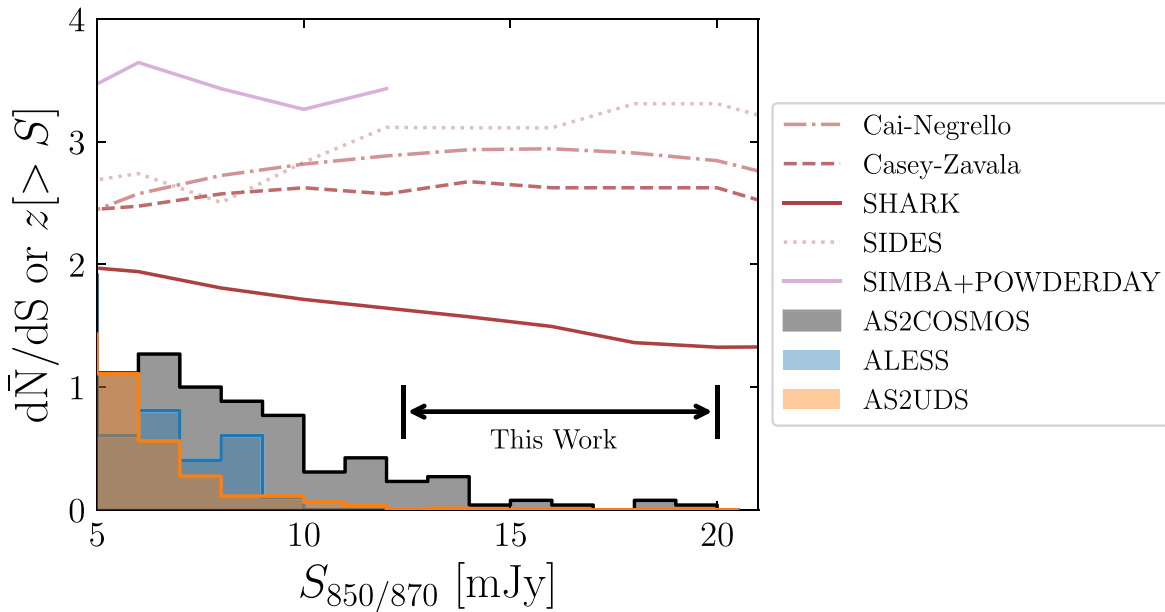


Figure 1. Predictions of median redshifts for SMGs with $850\ \mu\text{m}$ flux density (S_{850}) greater than certain flux cuts, based on empirical models of Cai–Negrello (Cai et al. 2013; Negrello et al. 2017), Casey–Zavala (Casey et al. 2018; Zavala et al. 2021), SIDES (B  thermin et al. 2017), the semianalytical model SHARK (Lagos et al. 2020), and the hydrodynamical simulation SIMBA (Dav   et al. 2019) coupled with dust radiative transfer modeling POWDERDAY (Lovell et al. 2021; Narayanan et al. 2021). At the bottom of the figure, we show the normalized histograms of three SMG samples that are constructed via a similar approach, meaning ALMA band 7 continuum follow-up observations on flux-limited samples of single-dish detected submillimeter sources. The histograms are arbitrarily normalized to show contrasts of different samples. Here AS2COSMOS (Simpson et al. 2020) has significantly more bright SMGs than AS2UDS (Stach et al. 2018) and ALESS (Hodge et al. 2013). The flux range presented in this work is indicated, which is ideal for redshift measurements thanks to its brightness and test model predictions.

Alexander & Hickox 2012; Toft et al. 2014; Dudzevi  t   et al. 2020). The fact that the massive ellipticals dominate the stellar mass budget among the local massive galaxies ($\gtrsim M_*$; Ilbert et al. 2013) suggests that the phases of SMGs could be responsible for the formation of most of their stellar masses (Thomas et al. 2010).

Their essential role in the formation and evolution of massive galaxies highlights how incredibly little we understand SMGs, even after the more than two decades since their first discovery (Smail et al. 1997; Barger et al. 1998; Hughes et al. 1998). Technical difficulties compounded with their extreme infrared luminosity have kept many issues unsettled regarding the basic physical properties of SMGs, both in theory and in observations. One issue, and arguably the only one, that has recently been considered more or less clear is the SMG number densities, or number counts. Observational results have now converged to within statistical uncertainties over a wide flux range after taking into account field-to-field variations (Karim et al. 2013; Simpson et al. 2015a, 2020; Oteo et al. 2016; Geach et al. 2017; Hill et al. 2018; Stach et al. 2018). However, this comes only after years of effort in examining the impact of multiplicity¹⁸ on counts deduced from single-dish measurements, which typically served as the basis of constructing the number counts (Wang et al. 2011; Barger et al. 2012; Chen et al. 2013; Hodge et al. 2013; Cowie et al. 2018). Models have also made significant progress, where measured number counts can now be reproduced, in many cases without having to invoke top-heavy stellar initial mass functions (Lacey et al. 2016; B  thermin et al. 2017; Safarzadeh et al. 2017; Casey et al. 2018; Lagos et al. 2020; Lovell et al. 2021). Note that top-heavy stellar initial mass functions

have been suggested in recent observational studies (Zhang et al. 2018; Dye et al. 2022). However, a variety of different techniques used to construct models has led to vastly different predictions on some of the most fundamental properties.

One outstanding example is redshift. While most models can reproduce the average redshift distribution (median of $z \sim 2.5$; Chapman et al. 2005) of typical SMGs with $850\ \mu\text{m}$ fluxes of $S_{850} \sim 2\text{--}9\ \text{mJy}$, they predict opposite trends and correlations toward the brighter end. One school of models predicts a median redshift of $z < 2$ at $S_{850} \gtrsim 9\ \text{mJy}$ (Lacey et al. 2016; Lagos et al. 2020), and another predicts a median $z > 3$ (Figure 1; B  thermin et al. 2017; Casey et al. 2018; Lovell et al. 2021). In addition, some models predict a more or less linear correlation between median redshift and S_{850} , but others have no such correlation. The differences in these predictions are likely due to different treatments of physical processes, such as the triggering of star and dust formation, or the adoption of phenomenological recipes driven by the observations themselves. Precise redshift measurements of bright SMG samples that are sufficiently large and complete would be powerful in testing these predictions and therefore represent the next frontier in understanding the formation of massive galaxies across cosmic time.

In the pre-Atacama Large Millimeter/submillimeter Array (ALMA) era, redshift measurements are focused on SMGs that in many cases have radio or mid-infrared detection, which was the technique used to identify their optical and near-infrared (OIR) counterparts after being discovered from single-dish submillimeter surveys (Ivison et al. 1998, 2007; Barger et al. 1999; Smail et al. 2000; Chapman et al. 2003, 2005; Wardlow et al. 2011; Umehata et al. 2014). Their redshifts were mostly estimated via simple flux ratios and, in some cases, OIR spectroscopic observations. They typically found a wide range of median redshifts in the range $z = 2\text{--}3$, with uncertainties on

¹⁸ Submillimeter sources uncovered by single-dish observations breaking into multiple constituent SMGs in follow-up interferometric observations.

the order of 10%–20%. In the ALMA era, where precise locations can be efficiently measured and counterpart identification is less biased, studies using well-defined samples have found more stable results of an overall median of $z \sim 2.5\text{--}2.6 \pm 0.1$, with a moderate increase in the median as a function of flux density (Simpson et al. 2014; Cowie et al. 2017; Stach et al. 2019). However, the majority of these redshifts are estimated via fittings of spectral energy distributions (SEDs); thus, any possible systematic offsets due to model assumptions need to be understood with spectroscopic redshift measurements.

Spectroscopic redshift measurements of SMGs are known to be difficult. With about 2 hr of exposures from 8–10 m class OIR telescopes, the line detection rates were found to be about $\sim 30\%$ (Casey et al. 2017; Cowie et al. 2017; Danielson et al. 2017). (Sub)millimeter spectral scan observations targeting bright CO and [C I] lines appear more feasible for SMGs that are dusty but interstellar medium (ISM) rich. Indeed, with a moderate time investment, this strategy has been successfully demonstrated on samples of very bright and typically strongly lensed sources discovered by Herschel or the South Pole Telescope (Vieira et al. 2013; Strandet et al. 2016; Bakx et al. 2020; Neri et al. 2020; Reuter et al. 2020; Urquhart et al. 2022). However, a general lack of these very bright ($S_{850} \gtrsim 25$ mJy) SMGs in models motivates similar observations to be conducted on fainter samples that are less influenced by gravitational lensing (Birkin et al. 2021; Jones et al. 2021).

Recently, Simpson et al. (2020) published an AS2COSMOS catalog of 260 SMGs that is based on subarcsecond ALMA band 7 continuum follow-up observations of the brightest 182 single-dish detected submillimeter sources ($S_{850} > 6.2$ mJy) drawn from the parent 1.6 deg^2 of the SCUBA-2 $850 \mu\text{m}$ survey in the COSMOS field (S2COSMOS; Simpson et al. 2019). Crucially, considering the depths of both the initial SCUBA-2 survey and the ALMA follow-up observations, the catalog provides ~ 20 and ~ 60 SMGs that are 100% and $>90\%$ complete at flux cuts of $S_{850} \sim 12$ and 9 mJy, respectively (Figure 1; Simpson et al. 2020). Under similar flux cuts, the bright subsamples are a factor of >3 and >50 larger than those of AS2UDS (Stach et al. 2019) and ALESS (Hodge et al. 2013), the two previous largest uniform ALMA follow-up SMG surveys, representing a major step forward in constructing a sizable and highly complete bright SMG sample. Together with the fact that the model predictions differ the most in this regime, the brightest SMGs (effectively high-redshift HyLIRGs) from AS2COSMOS provide an ideal test bed for constraining models (Figure 1).

Here we present the first results of an ALMA spectroscopic survey of the brightest AS2COSMOS SMGs, or AS2COSPEC. We present sample selection and the ALMA data in Section 2. In Section 3, we present the spectral extraction, as well as analyses on detailed modeling of the line profiles and redshift determinations. The implications and comparisons of our results are discussed in Section 4, and a summary is given in Section 5. Note throughout this paper that S_{850} and S_{870} are used to represent the flux measurements at the representative wavelengths of SCUBA-2 and ALMA band 7 observations, respectively. In reality, these measurements can be used interchangeably, given the current precision of flux measurements. We assume the Planck cosmology: $H_0 = 67.7 \text{ km s}^{-1} \text{ Mpc}^{-1}$, $\Omega_M = 0.31$, and $\Omega_\Lambda = 0.69$ (Planck Collaboration et al. 2020).

2. Observations and Data

2.1. Sample

Our sample is drawn from AS2COSMOS, a parent sample of 260 SMGs identified by ALMA band 7 continuum follow-up observations of a highly complete (99.5%), flux-limited ($S_{850} > 6.2$ mJy) sample of the brightest submillimeter sources uncovered by the single-dish S2COSMOS over an area of 1.6 deg^2 (Simpson et al. 2019, 2020). The ALMA band 3 observations presented in this paper targeted the brightest 18 AS2COSMOS SMGs that are at the flux range of $S_{870} = 12.4\text{--}19.3$ mJy based on the ALMA measurements (Simpson et al. 2020). The main goals are to measure the redshift distributions and gravitational lensing magnifications and study the ISM properties via molecular lines such as CO and [C I]. Comparing to the previous large samples of ALMA-identified SMGs from follow-up observations of single-dish detected submillimeter sources, in Figure 1, we show that there are only two SMGs that are similarly bright as our sample in the AS2UDS sample (Stach et al. 2018), and there are none in the ALESS sample (Hodge et al. 2013). Note that about one-third of the sample was observed in the millimeter by NOEMA and other ALMA data sets, and their measured redshifts were reported by Jiménez-Andrade et al. (2020), Simpson et al. (2020), and Birkin et al. (2021), which are consistent with our results.

2.2. ALMA Data

The data were taken in 2019 November and December under project number 2019.1.01600.S. The observations were split into 11 execution blocks, each of which amounts about 1.5 hr worth of data for both science and calibrations. The default spectral scan setup was adopted in the ALMA Observing Tool, meaning that each execution block contains data on all 18 SMGs with five spectral tunings continuously covering from 84.1 to 113.3 GHz (Figure 2), where each tuning with four spectral windows was carried out for exactly 26 s. That is, across the whole frequency range observed, each spectral channel received a total of about 4.8 minutes (26 s times 11 executions) of science data on each SMG, except in the range of 97.7–101.3 GHz, as well as overlapping edge channels, where the on-target exposure time roughly doubles. Each spectral window is tuned to a standard time division mode with 128 channels and a frequency width of 15.625 MHz, corresponding to a velocity width of about $40\text{--}55 \text{ km s}^{-1}$, depending on the observed frequency. At least 43 and up to 49 antennas were used for each execution block, with a baseline length ranging from 15 to 313 m, hence a nominal C43-2 configuration. Since the target SMGs are all located in the COSMOS field, the phase calibrator was always J1008+0029, and J1037-2934 was always used for the amplitude and bandpass calibrations. The weather conditions during these observations were standard band 3 weather, with precipitable water vapor ranging from 1.7 to 5.8 mm.

We adopt the calibrations performed in the second level of quality assurance (QA2). Flagging and calibrations were done using CASA pipeline version 5.6.1-8, which is also the version used for imaging. Additional manual flags were put in by the QA2 team to remove antennas or scans with poor performance, in particular, a line at 91.66 GHz leaking from the local oscillator water vapor radiometer, which is marked in Figure 2. We reviewed the weblog record and confirmed the quality of the calibration results.

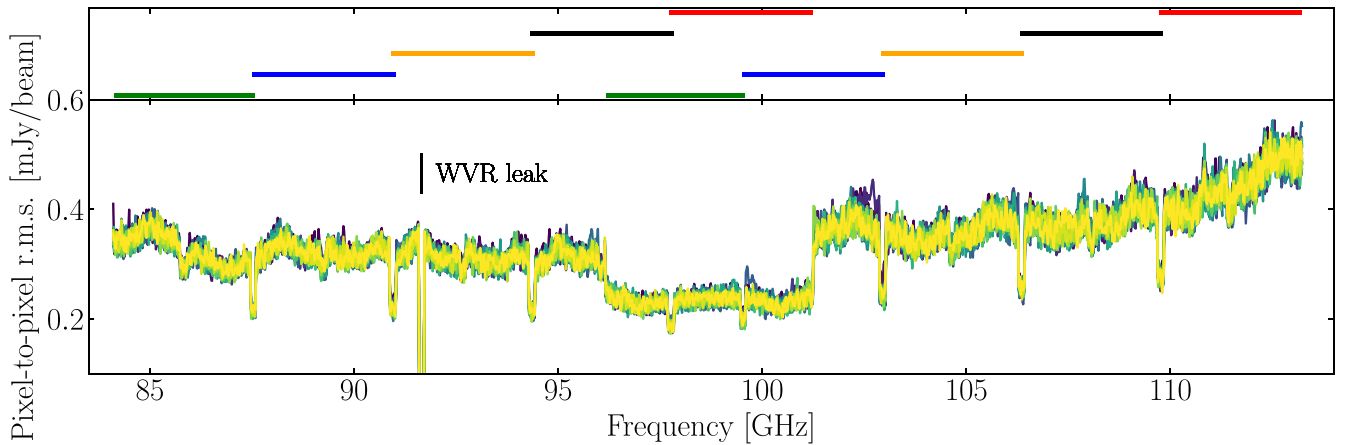


Figure 2. Top: spectral coverage of the five sets of tuning adopted for our ALMA observations, where each set is plotted with the same color. Bottom: spectral sensitivity curves of our ALMA data expressed in pixel-to-pixel rms, which are made based on data cubes smoothed to a common uniform beam size and shape. The curves of all 18 sources are plotted, with each being assigned to a random brightness of green to show the small scatter (a few percent) of data quality among each of our sample sources thanks to the observing strategy. The overall rms median is $0.33 \text{ mJy beam}^{-1}$ per 15.6 MHz ($\sim 40\text{--}55 \text{ km s}^{-1}$), with notable dips due to overlaps of spectral coverage between different tunings, except for the marked position due to the Water Vapor Radiometer (WVR) leak, which was flagged during the QA2 process.

To image the visibilities, the calibrated visibilities were first continuum-subtracted. To do that, the channels that contain line emissions need to be excluded for a proper first-order continuum fitting. The line channels to be masked were determined from the spectra extracted from the delivered pipeline-produced imaging cubes through typical single Gaussian fitting spanning $\pm 3\sigma$ centered at the Gaussian peaks based on the fits. The spectra were extracted using circular apertures centered at the $870 \mu\text{m}$ continuum positions (the phase centers), and their radius were determined by a curve-of-growth method.

We then used TCLEAN to inverse Fourier transform and clean the continuum-subtracted visibilities. The visibilities were transformed to image cubes of 270×270 pixels in the x - (R.A.) and y - (decl.) axes with a pixel size of $0''.42$ ($\sim 6\text{--}8$ pixels per synthesized beam) and 1870 channels in the z - (frequency) axis. We adopt natural baseline weighting across all spectral windows in order to maximize the signal-to-noise ratio (S/N) for line detection. To increase the efficiency of clean, we adopted the automasking approach (Kepley et al. 2020) in TCLEAN, which allows CASA to generate masks for each channel in an iterative process based on a few parameters. To do that, we set the *usemask* parameter to “auto-multithresh.” For each channel, the first round of mask creation only includes pixels with an S/N of 4 and above (*noisethreshold* = 4), and then the mask is allowed to expand in order to include lower-S/N regions (*lownoisethreshold* = 2.5). The masked regions determined by automasking are then cleaned down to the 2σ level (*nsigma* = 2 in TCLEAN). Examples of the cleaned channels and their associated masks are shown in Figure 3. Finally, given the same baseline weighting across the whole frequency range, the spatial resolution of each frequency channel differs slightly, up to $\sim 35\%$ end-to-end. To allow more straightforward analyses and understanding of the data, we applied smoothing on the reduced cubes by using the CASA routine IMSMOOTH, setting the kernel to the common resolution, which is normally the largest beam size of the presmoothed cube. After this step, the spatial resolution of all cubes is uniform, with a synthesized beam FWHM of $4''.3 \times 3''.5$ and a small P.A. range of $69^\circ\text{--}72^\circ$. The final spectral sensitivity achieved is uniform across all sources to within a few percent, thanks to the observing strategy; however, it differs among channels mainly due to the tuning coverage. We show the

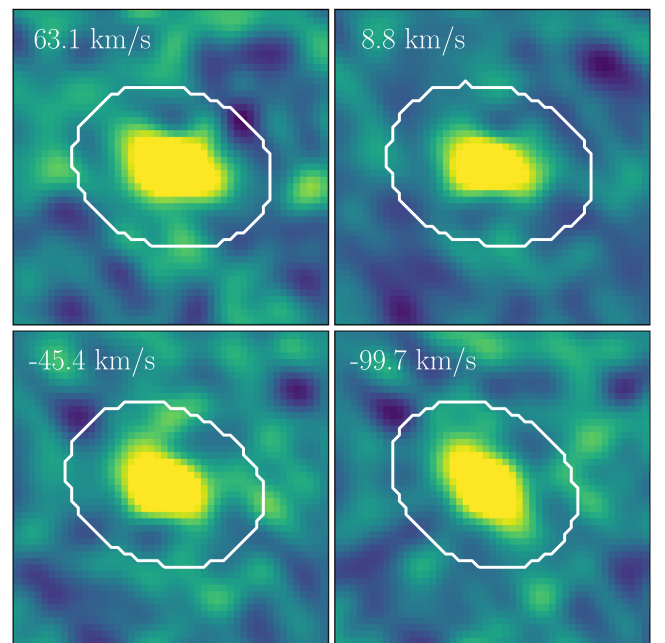


Figure 3. Example of channel maps of AS2COS0023.1, each $20''$ on a side, where the velocities are referenced to the systemic redshift. The masked regions for TCLEAN are enclosed within the white curves. This demonstrates the flexibility of automasking in TCLEAN.

pixel-to-pixel rms in Figure 2, and the overall median is $0.33 \text{ mJy beam}^{-1}$ per 15.6 MHz ($\sim 40\text{--}55 \text{ km s}^{-1}$). The continuum of each source was also imaged with natural weighting, resulting in images with a synthesized beam FWHM of $3''.6 \times 3''.0$ and a small P.A. range of $77^\circ\text{--}80^\circ$. The sensitivity achieved for the continuum is also uniform across different sources, $12\text{--}13 \mu\text{Jy beam}^{-1}$ at the representative frequency of 98.7 GHz .

3. Analyses and Results

3.1. Line Detection and Spectrum Extraction

To systematically search for line emission and quantify its significance, we ran the publicly available code LINESEEKER,

which was first written and used to search for line emission for the ALMA frontier field survey (González-López et al. 2017) and later applied to the data taken for the ALMA Spectroscopic Survey in the Hubble Ultra Deep Field (Walter et al. 2016; González-López et al. 2019). LINESEEKER utilizes a matched filtering technique that combines spectral channels based on Gaussian kernels with a range of widths. The widths are chosen to match lines detected in real observations. The line candidates are determined to be significantly detected if their S/Ns are larger than the most significantly detected negative signals in the cube, and we find that a significance threshold of $S/N > 10$ satisfies the aforementioned requirement in all cases. In this paper, we focus on the spectra of the known SMGs in the AS2COSMOS catalog (Simpson et al. 2020), and the results from the search of serendipitous detection will be presented in a future work. For the 18 primary SMGs, 17 have yielded significant line detection based on LINESEEKER, and AS2COS0037.1 is the only source that has none.

The spectra used for later analyses are extracted based on the coordinates presented in Simpson et al. (2020), which are based on ALMA 870 μm continuum observations. All of our targets have their 3 mm continuum detected, and we confirm that via 2D elliptical Gaussian fitting using IMFIT. The coordinates of the 3 mm continuum best-fit peaks are consistent with those of the 870 μm continuum. We therefore adopt the 870 μm coordinates, given the significantly lower positional uncertainties. The results of IMFIT also suggest that the 3 mm continuum is not spatially resolved, which is expected, since no strongly lensed SMGs like our targets are typically found to have subarcsecond sizes in the rest-frame submillimeter (e.g., Ikarashi et al. 2015; Simpson et al. 2015b; Hodge et al. 2016, 2019; Chen et al. 2017; Fujimoto et al. 2018; Gullberg et al. 2019).

To determine the optimal aperture size for extracting the spectra and to derive the total line flux density, we employ curve-of-growth analyses at the frequency of the emission lines and using the continuum-subtracted cubes. For each source, spectra are extracted based on a set of apertures that are centered at the 870 μm continuum position, shaped as a synthesized beam, and scaled by a range of factors in beam size from 0.5 to 4.5 with steps of 0.25. To estimate the line flux density, we conduct χ^2 model fitting for each spectrum extracted, and two models, single and double Gaussian, are considered. Given the channel-to-channel variations in sensitivity, the fittings are weighted by the noise of each spectral channel, which is estimated by taking the standard deviation of a collection of 1000 flux density measurements at random positions at same frequency but with the same aperture as that used to extract the target spectra. The line flux density of each extracted spectrum is then computed by integrating the best-fit model curves.

Because of the two adopted Gaussian models, the above approach results in two curve-of-growth curves for each target SMG. The selected examples are shown in Figure 4, in which we can first observe that the integrated line flux densities are not sensitive to the different underlying models. Second, while some curves converge to a certain flux density level, as expected from a curve-of-growth analysis, some appear not to be converging. We suspect that this is due to larger-scale noise structures, which has also been shown to be the case in other ALMA data sets (e.g., Novak et al. 2020). Indeed, by taking the median of all of the curves (one from each target SMG)

normalized at a given aperture size, one beam in this case, we find that this median curve nicely converges beyond around three times the beam size. In addition, this converging median curve is stable to within a few percent against the choice of aperture size to which all of the curves are normalized, suggesting that this median curve can be used as a common profile for correcting the line-integrated flux densities to total. Note that there is a hint of extended emission by comparing the median curve to the curve of growth of the synthesized beam, although the difference is not significant (Figure 4). The detailed size analyses will be presented in a forthcoming paper. However, to account for this possible extended emission, we adopt the median curve instead of the curve of the synthesized beam for the correction to total (the difference is $\sim 20\% \pm 10\%$). We adopt the aperture equivalent to one synthesized beam partly because all of the curves appear to be stable until this point, beyond which they start to diverge (Figure 4). It also yields higher-S/N spectra compared to those extracted with larger aperture sizes, which helps to determine a more appropriate model for the spectral profile (Section 3.2).

Given the above justifications, the spectra that we use for analyses from this point on are therefore extracted using the aperture equivalent to the synthesized beam, and their estimated line flux densities are corrected to total based on the median of the curve-of-growth curves. For AS2COS0001.1, AS2COS0008.1, and AS2COS0028.1, where the nearby SMGs are also detected in a few cases and close enough to potentially affect the spectra, we reimage the cubes using the Briggs baseline weighting with a robust parameter of -1.5 ,¹⁹ resulting into an $\sim 35\%$ reduction of the beam size, allowing clear separations to the companions with at least one synthesized beam distance ($\sim 3''$). The spectra of these three SMGs are then extracted based on the smaller beam and again corrected to total using the corresponding median curve.²⁰ Finally, for AS2COS0037.1, the only target SMG for which we do not obtain significant line detection, the spectrum is extracted using the synthesized beam, but no correction to total is applied. An overview of all 18 spectra is shown in Figure 5, where we also show the error-weighted stacked spectrum in S/N. No additional emission lines are detected in the stacked spectrum. We have also experimented with luminosity-weighted and luminosity-normalized stacking; however, the results remain unchanged.

3.2. Model Fitting

The first analysis we perform on the extracted spectra is to determine which model, single or double Gaussian, better describes the data. To make a quantitative assessment, we employ both the Bayesian information criterion (BIC) and a version of the Akaike information criterion (AIC) that is modified for the limited sample size (AICc). The analyses are documented in Appendix A, and the best-fit models are shown in Figure 6. In general, we find that the results based on BIC and AICc are consistent with each other in 80% of the cases, and they all point toward the fact that about 90% of the primary SMGs have lines that are better described by double Gaussian profiles. The implications of this result are addressed in the discussion section.

¹⁹ We have also tried uniform weighting, but some spectra became too noisy. The current setting represents a good balance between spatial resolution and S/N.

²⁰ The curve-of-growth analyses were rerun to all sources with the same weighting.

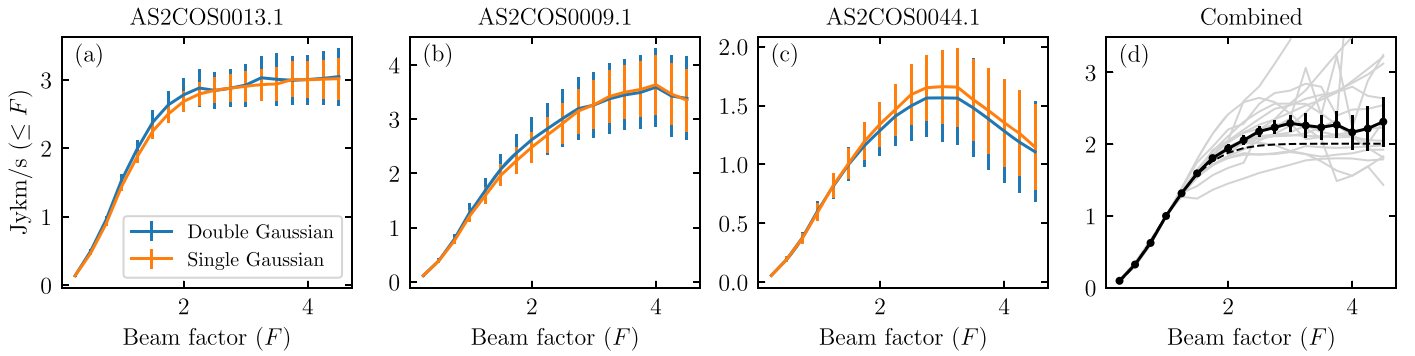


Figure 4. Example results of the curve-of-growth analyses, showing the curves converging (a), monotonically increasing (b), and downturning (c) as a function of the size of the synthesized beam. Results from the single and double Gaussian models are both shown, as indicated in the legend. In panel (d), we show that by normalizing all curves to a beam factor of 1 (gray), the median curve (solid) with the bootstrapped uncertainties appears stable and converging, which is consistent with the shape of the synthesized beam (dashed) and showing that the nonconverging behavior of individual targets could be due to larger-scale noise structures. We therefore, in principle, adopt the synthesized beam as the aperture to extract spectra and use this median curve to correct the measured flux densities to total. Note that this median curve is stable to within a few percent against the choice of aperture size to which all of the curves are normalized.

Moment calculations are adopted to compute line properties using best-fit single and double Gaussian models, meaning

$$\begin{aligned}\bar{I} &= \int I_\nu d\nu \\ \bar{\nu} &= \frac{\int \nu I_\nu d\nu}{\int I_\nu d\nu} \\ \bar{\sigma} &= \frac{\int (\nu - \bar{\nu})^2 I_\nu d\nu}{\int I_\nu d\nu}\end{aligned}$$

and the first moment ($\bar{\nu}$), i.e., intensity-weighted central frequencies, are used to determine redshifts. The zeroth and second moments will be used in a forthcoming paper to discuss the line properties in detail.

3.3. Redshift Determination

To determine redshifts, the target SMGs are grouped into three categories: SMGs with multiple line detection, those with only one line detection, and those that do not have emission line detection. Other works in the literature are referenced to aid the redshift determinations, in particular those from Jiménez-Andrade et al. (2020), Mitsuhashi et al. (2021), and Daddi et al. (2022). The category to which each SMG belongs is given in Table 1. In total, 10 (56%) SMGs have their redshifts determined by multiple emission lines, seven (39%) by a single emission line, and one (6%) by its photometric redshift.

For the SMGs with multiple line detections, the measured line frequencies are cross-matched to combinations of redshifted emission lines, considering species that typically emit strongly at the submillimeter, such as carbon monoxide (CO) and atomic carbon ([C I]). We find a unique combination for each SMG, and the results are listed in Table 1. The final adopted redshifts are determined in two ways. If the SMGs have multiple line detections in this reported ALMA data set, their redshifts are determined by taking a weighted average of the redshift solutions of each line. If the second line detection originated from other work in the literature, we adopt our measurements, since they tend to have higher precision.

For the SMGs that only have one line detection, we find the solutions that are best matched to the photometric redshifts

reported in S. Ikarashi et al. (in preparation), where, as in Dudzevičiūtė et al. (2020), the SED code MAGPHYS is employed. We assume the line to be one of the CO transitions, which is justified by the fact that the frequency coverage of our data would have covered a CO line if the line was instead [C I]. Since in SMGs, [C I] is typically weaker than the nearby CO lines ($J_{\text{up}} = 4, 5$; Spilker et al. 2014; Birkin et al. 2021), if the line is [C I], then the nearby CO lines would have been detected. We note that, compared to other methods, MAGPHYS has the advantage of taking into account far-infrared and submillimeter photometry, allowing redshift estimates for all AS2COSMOS SMGs, which are often faint or undetected in OIR wave bands, which the known COSMOS catalogs such as COSMOS2015 (Laigle et al. 2016) and COSMOS2020 (Weaver et al. 2022) are based on. However, given the rich information provided in the COSMOS catalogs, a good number of matches can be found on our target SMGs; we nevertheless exploit them later for detailed assessments.

Lastly, for the only SMG that has no line detection, AS2COS0037.1, the photometric redshift reported by S. Ikarashi et al. (in preparation), as well as the latest COSMOS2020 catalog ($1.93_{-0.07}^{+0.04}$ and $1.98_{-0.15}^{+0.03}$ based on the LePhare and EAZY codes, respectively; Weaver et al. 2022), suggest that this SMG could be located within the known redshift gap of the ALMA band 3 spectral scan, which is $z = 1.74\text{--}2.05$. Indeed, given the depth reached by our data ($\sim 0.3 \text{ mJy beam}^{-1}$), assuming a single Gaussian model of a 3σ peak and a typical line width of 500 km s^{-1} , the line intensity limit is 0.5 Jy km s^{-1} . Assuming the missing line is CO(3–2), the closest transition based on the photometric redshift, the line intensity limit corresponds to a limit on the CO(1–0) luminosity of $L'_{\text{CO}(1-0)} = (2\text{--}4) \times 10^{10} \text{ K km s}^{-1} \text{ pc}^2$, assuming the latest $r_{31} \equiv L'_{\text{CO}(3-2)}/L'_{\text{CO}(1-0)} = 0.63$ (Birkin et al. 2021). Given the infrared luminosity of $\sim 10^{13} L_\odot$ (C.-L. Liao et al. 2022, in preparation), this luminosity limit is well below the measured $L_{\text{IR}}\text{--}L'_{\text{CO}(1-0)}$ correlation and would have allowed detection of the line in $\gtrsim 90\%$ of the literature reported detection on SMGs (Birkin et al. 2021). We therefore adopt 1.90 ± 0.05 for AS2COS0037.1, which is simply the mean of the redshift gap with an uncertainty that makes the probability of it being outside the redshift gap equivalent to 3σ .

In Table 1, we report the redshift solutions of our sample on individual lines, as well as the final adopted values for each SMG, based on the methods stated above. We adopt the

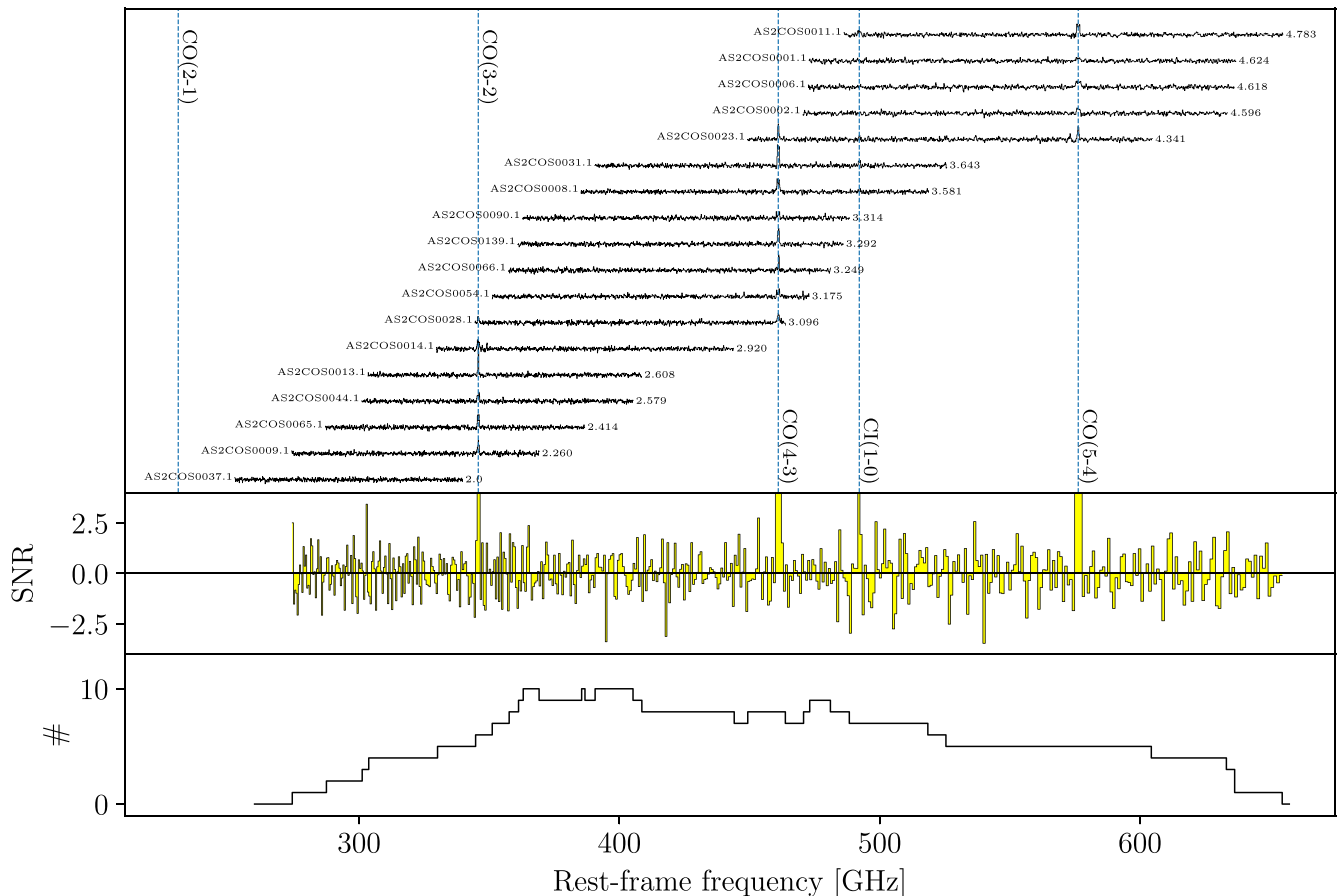


Figure 5. Top: overview of the continuum-subtracted spectra of all 18 primary SMGs in their rest-frame frequencies, along with the marked locations of strong molecular and atomic lines. Spectral lines are detected in 17 out of 18 targeted SMGs. The SMGs with a single line detection have their redshifts determined jointly with photometric redshifts, which can be shown to have an $\sim 70\%$ – 80% success rate based on those that have multiple line detections (Section 3.3; Birkin et al. 2021). The only SMG that is bright in OIR but has no lines detected in the scan is AS2COS0037.1, suggesting that, based on its photometric redshift, it is likely sitting within the known redshift gap for the band 3 scan. In this plot, we therefore set the redshift of AS2COS0037.1 to 2.0 for demonstration purposes. Middle: error-weighted stacked spectrum in S/N, binned to $500 \text{ km s}^{-1} \text{ channel}^{-1}$. The range in y-axis is from -4 to 4 ; AS2COS0037.1 is not included in the stack. No additional lines are detected in the stacked spectrum. Bottom: number of spectra involved in the stack for each channel.

redshift results based on the selected model for each SMG listed in Table A1, although we note that these results are not sensitive to the chosen single or double Gaussian models for the line fitting.

In Figure 7, we compare the photometric and adopted spectroscopic redshifts for all target SMGs except for AS2COS0037.1. We find that based on the 10 SMGs that have multiple line detection, three sources have their spectroscopic redshifts differ from photometric redshifts by more than 1, effectively meaning that if only a single line were detected, it would have been assigned to an incorrect CO transition based on photometric redshifts. This suggests a 70% success rate for our strategy of using photometric redshifts to aid in determinations of spectroscopic redshifts for SMGs with a single line detection. However, note that this success rate is estimated based on the higher-redshift subset, which tends to have less reliable photometric redshifts. Thus, the success rate for our sample SMGs that have a single line detection could be higher.

Our success rate is similar to that of a recent blind survey of emission lines on fainter SMGs (Birkin et al. 2021), in which they found about an 80% success rate. Excluding the three outliers, we find that the median redshift difference is $\langle \Delta z / (1 + z_{\text{spec}}) \rangle = 0.04 \pm 0.04$ with a bootstrapped error and a scatter of $\sigma_{\Delta z / (1 + z_{\text{spec}})} = 0.06$, suggesting that the photometric redshifts

estimated via SED fitting using MAGPHYS can be accurate, on average, with good precision. However, we also find that the scatter is much larger than what can be inferred from the quoted uncertainties of the photometric redshifts, indicating that the uncertainties of the photometric redshifts are underestimated.

Based on the assessments above, we expect that for the seven SMGs that have only one line detection, about one to two sources may have their real redshifts different from, and likely higher than, the adopted values (details given in Appendix B). We take these into account when comparing our results to model predictions.

4. Discussion

4.1. Physically Associated Pairs

Interferometric follow-up observations in the past decade have convincingly shown that submillimeter sources detected by single-dish observations tend to break up into multiple sources with a probability strongly correlated with the flux density of single-dish measurements, from $\sim 10\%$ for $\sim 3 \text{ mJy}$ SMGs to $>50\%$ for SMGs at $\gtrsim 10 \text{ mJy}$ (Wang et al. 2011; Barger et al. 2012; Hodge et al. 2013; Simpson et al. 2015a, 2020; Cowie et al. 2018; Hill et al. 2018; Stach et al. 2019). While the number of constituent SMGs can range from two to four, it has

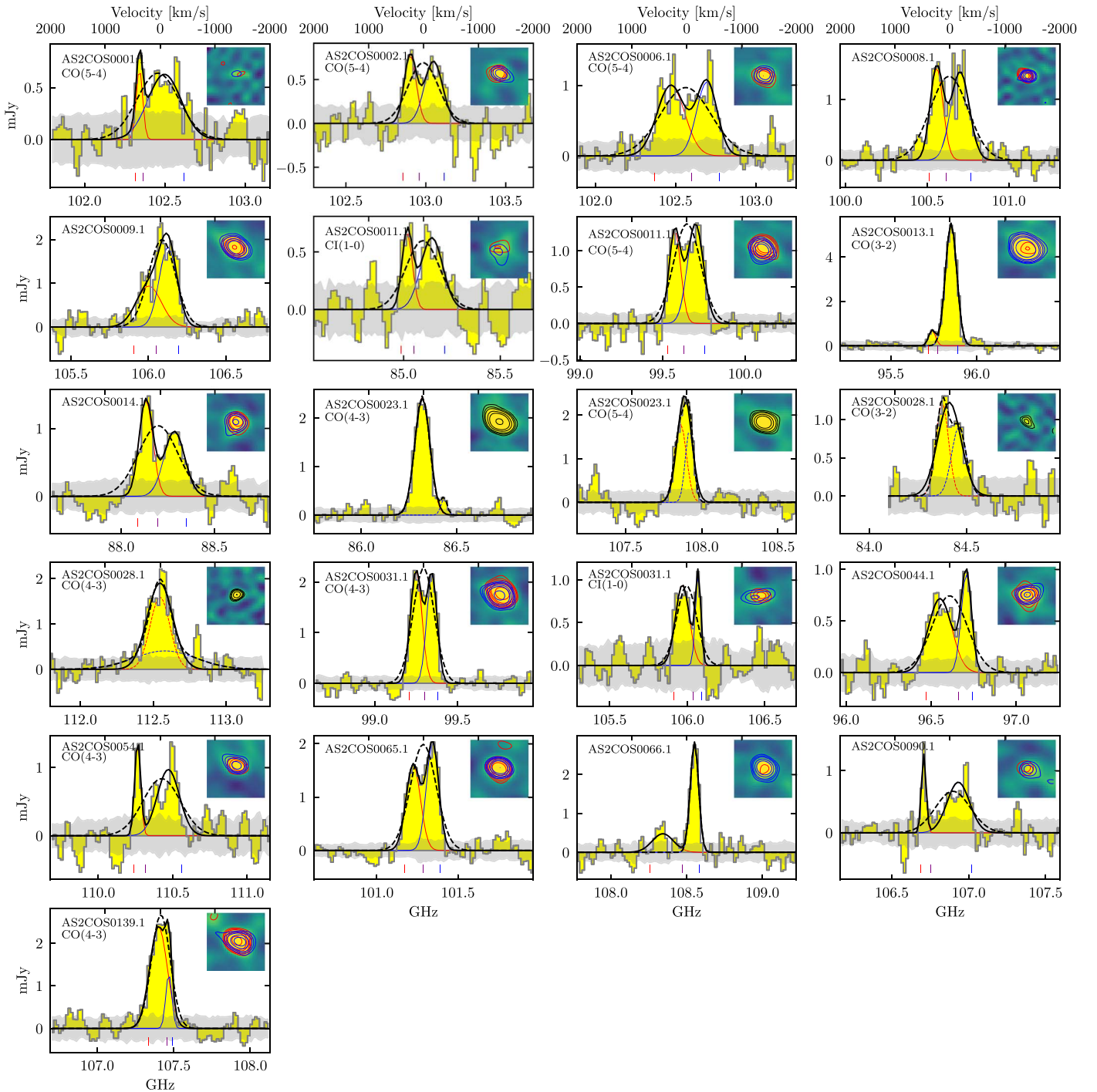


Figure 6. Spectra of all of the detected line emissions from our primary SMGs, with their IDs indicated. All spectra are extracted using the aperture equivalent to the synthesized beam and centered on the line centers of the best-fit models. The range of frequency plotted corresponds to a velocity range of ± 2000 km s $^{-1}$. The best-fit single and double Gaussian models are plotted with dashed and solid curves, where the preferred models according to Table A1 are plotted with solid. The red and blue components of the double Gaussian models are also shown. The gray bands indicate the rms levels. The transition of the line is also indicated if the redshift of the corresponding SMG is confirmed with more than one emission line. The inset of each spectrum shows the velocity-integrated emission over the line FWHM, and it is shown in S/N linearly scaled from -4 to 6 with a box size of $12'' \times 6$ on a side. The contours are plotted at levels of $[3, 4, 5, 7, 9, 15]\sigma$; they are in black if a single Gaussian model is preferred or red and blue if a double Gaussian model is selected. The small ticks below the lines that are better described by double Gaussian models mark the frequency ranges for making the velocity-integrated signals for the red and blue components.

also been shown that the flux densities measured from single-ish observations are dominated by the brightest constituent SMG, with a 70% contribution, on average.

The relationship among these constituent SMGs is, however, unclear, in particular whether they are physically associated and undergoing dynamical interactions or unrelated SMGs that

are simply a result of line-of-sight chance projections. The determination of this relationship has profound implications in our understanding of the triggering mechanisms of star formation for SMGs. Observationally, statistical approaches using photometric redshifts and number density analyses have suggested that $\sim 30\%$ of these pairs are physically associated

Table 1
Redshifts of the Primary Target SMGs

ID	z_{phot}	N_L^a	Line	z_{spec}^b	$z_{\text{spec,adopted}}^c$	Other Lines
AS2COS0001.1	2.52+0.21-0.16	ML	CO(5–4)	4.6237 ± 0.0007	4.6237 ± 0.0007	[C II] ^d
AS2COS0002.1	4.71+0.61-0.00	ML	CO(5–4)	4.5956 ± 0.0006	4.5956 ± 0.0006	[C II] ^d
AS2COS0006.1	3.52+0.00-0.06	ML	CO(5–4)	4.6183 ± 0.0001	4.6183 ± 0.0001	[C II] ^d
AS2COS0008.1	3.35+0.05-0.17	SL	CO(4–3)	3.5811 ± 0.0004	3.5811 ± 0.0004	
AS2COS0009.1	2.67+0.00-0.04	SL	CO(3–2)	2.2599 ± 0.0002	2.2599 ± 0.0002	
AS2COS0011.1	4.29+0.66-0.41	ML	C I(1–0)	4.7831 ± 0.0007	4.7830 ± 0.0002	
			CO(5–4)	4.7830 ± 0.0002		
AS2COS0013.1	2.46+0.02-0.05	ML	CO(3–2)	2.6079 ± 0.0001	2.6079 ± 0.0001	CO(1–0) ^e
AS2COS0014.1	3.25+0.02-0.10	SL	CO(3–2)	2.9202 ± 0.0005	2.9202 ± 0.0005	
AS2COS0023.1	4.43+0.00-0.00	ML	CO(4–3)	4.3410 ± 0.0001	4.3411 ± 0.0001	CO(1–0) ^e
			CO(5–4)	4.3414 ± 0.0002		
AS2COS0028.1	3.40+0.06-0.17	ML	CO(3–2)	3.0966 ± 0.0003	3.0965 ± 0.0002	
			CO(4–3)	3.0964 ± 0.0002		
AS2COS0031.1	3.31+0.00-0.00	ML	CO(4–3)	3.6432 ± 0.0001	3.6432 ± 0.0001	CO(1–0) ^e
			C I(1–0)	3.6431 ± 0.0004		
AS2COS0037.1	2.35+0.04-0.02	NL			1.90 ± 0.05	
AS2COS0044.1	2.98+0.14-0.05	SL	CO(3–2)	2.5793 ± 0.0002	2.5793 ± 0.0002	
AS2COS0054.1	2.73+0.00-0.00	ML	CO(4–3)	3.1755 ± 0.0004	3.1755 ± 0.0004	CO(1–0) ^e
AS2COS0065.1	2.40+0.29-0.01	SL	CO(3–2)	2.4140 ± 0.0002	2.4140 ± 0.0002	
AS2COS0066.1	2.90+0.06-0.06	SL	CO(4–3)	3.2492 ± 0.0005	3.2492 ± 0.0005	
AS2COS0090.1	3.48+0.85-0.11	SL	CO(4–3)	3.3137 ± 0.0003	3.3137 ± 0.0003	
AS2COS0139.1	2.23+0.00-0.02	ML	CO(4–3)	3.2923 ± 0.0002	3.2923 ± 0.0002	Ly α ^f

Notes.

^a Number of lines detected, where ML stands for multiple lines, SL for a single line, and NL for no line.

^b Redshift solutions for each line.

^c Redshift solutions for each source.

^d Mitsuhashi et al. (2021).

^e F. Castillo et al. (2022, in preparation).

^f Daddi et al. (2022).

(e.g., Stach et al. 2018; Simpson et al. 2020), which is in agreement with spectroscopic measurements of small samples of paired SMGs (Hayward et al. 2018; Wardlow et al. 2018). Theoretically, models have instead predicted that the majority of these pairs are physically unassociated, especially for the bright submillimeter sources with a single-dish measured flux density of $S_{850} \gtrsim 10$ mJy (Hayward et al. 2013a; Cowley et al. 2015; Muñoz Arancibia et al. 2015). To definitely settle this issue, spectroscopic follow-up observations are needed, and our sensitive spectral measurements on a complete sample of bright SMGs are suitable for providing further constraints.

Our sample include five pairs of SMGs, and their 870 μm continuum images and 3 mm spectra are shown in Figure 8. As stated in Section 3.1 and seen in Figure 8, the spatial resolutions of the naturally weighted cubes are too coarse to separate the SMG pairs of AS2COS0001.1/1.2, AS2COS0008.1/8.2, and AS2COS0028.1/28.2. We therefore reimage those cubes using Briggs weighting with a robust parameter of -1.5 , which stands as a good balance between sensitivity and resolution after experimenting with different baseline weightings. To increase the detectability of line emission, we also binned the channels to $\sim 150 \text{ km s}^{-1} \text{ channel}^{-1}$, appropriate for the typical line width of SMGs, which is about 500 km s^{-1} in FWHM (e.g., Bothwell et al. 2013; Birkin et al. 2021). The spectra are extracted using apertures centered on their reported 870 μm locations (Simpson et al. 2020) with the sizes and shapes of their corresponding synthesized beams, shown in the corners of Figure 8.

We obtain a significant detection from AS2COS0008.2 and a marginal detection from AS2COS0001.2. The best-fit single Gaussian model suggests that the redshift of AS2COS0008.2 is

3.5739 ± 0.0009 , assuming that it is the same line as AS2COS0008.1, and the significance of the detection is at $>4\sigma$ based on the velocity-integrated intensity over the FWHM of the best-fit model (Figure 8). Although marginal ($\sim 2\sigma$ over the FWHM) in our data, the same line from AS2COS0001.2 (and AS2COS0001.1) was detected at high significance ($>5\sigma$) by Jiménez-Andrade et al. (2020) with much deeper data from NOEMA, and Simpson et al. (2020) and Mitsuhashi et al. (2021) both reported detection of the [C II] line from AS2COS0001.2. Their reported redshifts are consistent with our measurements. For the following analyses, we therefore adopt the redshift measured by Jiménez-Andrade et al. (2020) for AS2COS0001.2, which is 4.633 ± 0.001 .

The velocity differences between these two pairs are within 500 km s^{-1} . At the projected distances of 20–30 kpc, their velocity differences would suggest that these two pairs are gravitationally bound systems, assuming that SMGs as suggested by clustering analyses reside within halos with masses of $\sim 10^{13} M_{\odot}$ (Hickox et al. 2012; Chen et al. 2016; Wilkinson et al. 2017; An et al. 2019; Lim et al. 2020; Stach et al. 2021). The redshift differences of the two pairs are both $\Delta z < 0.02$, a definition adopted by some models for physically associated pairs (Hayward et al. 2013a; Muñoz Arancibia et al. 2015). This suggests that 40% of the paired SMGs in our sample are physically associated. In addition, given that our observations are designed to detect lines from bright SMGs, deeper observations may reveal associated line emissions from the secondary SMGs of other pairs, and the true fraction of physically associated pairs could be higher. Indeed, as seen in Figure 8, among these four secondary SMGs, those not detected in line by our data are the

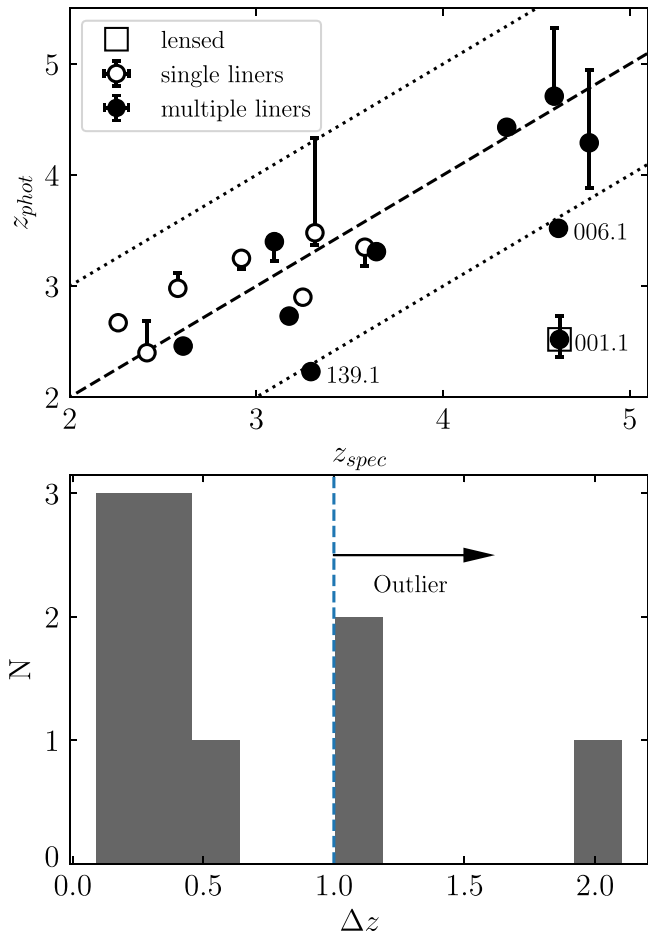


Figure 7. Top: comparisons between photometric and spectroscopic redshifts of the 17 primary SMGs that are detected in lines, where the dashed line shows the one-to-one relation and the two dotted lines show $\Delta z \equiv |z_{\text{photo}} - z_{\text{spec}}| = 1$, outside of which is considered an outlier. The outliers are defined as those with $\Delta z > 1$, meaning that if only a single line is detected, it is assigned to an incorrect CO transition based on photometric redshifts. The ID numbers of the two outliers are indicated. The SMGs that have multiple lines detected are marked as filled circles, and those with only one line detected are marked as open ones. The one that is boxed is AS2COS0001.1, because its photometry could be contaminated by a nearby foreground lens galaxy. Bottom: histogram of the differences between the photometric and spectroscopic redshifts (Δz) based on SMGs that have multiple lines detected. Excluding the two outliers, we find that the median redshift difference is $\langle \Delta z / (1 + z_{\text{spec}}) \rangle = 0.04 \pm 0.04$ with a bootstrapped error.

faintest in $870 \mu\text{m}$ flux densities ($< 2 \text{ mJy}$), and based on recent measurements (Dudzevičiūtė et al. 2020; Birkin et al. 2021), we do not expect to detect lines on these faint SMGs given the sensitivity of our data. Our results are also consistent with Simpson et al. (2020), where, based on the number counts analyses, they estimated that $62\% \pm 7\%$ of the $> 3 \text{ mJy}$ secondaries are physically associated with the primary SMGs.

While our results suggest a relatively high fraction ($\geq 40\%$) of physically associated SMG pairs, the current sample size is admittedly too small to have much constraining power. Furthermore, it is also not straightforward to compare our results against model predictions. First of all, the adopted criteria in defining pairs are different in each model. For example, Cowley et al. (2015) made predictions based on the brightest two constituent SMGs. On the other hand, Hayward et al. (2013a) considered all SMGs with $850 \mu\text{m}$ flux densities of $> 1 \text{ mJy}$, which is the flux level that is highly incomplete in the parent AS2COSMOS catalog. Second, our spectral measurements are

incomplete in terms of including all pairs or multiples of submillimeter sources above a certain flux density limit measured by SCUBA-2,²¹ which is what model predictions are typically based on. To make fair comparisons, experiments that are tailored for these model predictions are needed.

In spite of these caveats, however, our results do provide constraints on this issue from another angle. Since our target SMGs are complete to their flux cuts, it can be stated that our results suggest that for SMGs brighter than 12.4 mJy at $870 \mu\text{m}$, their brightest companion SMGs are physically associated with the primary SMGs $\geq 40\%$ of the time.

4.2. Redshift Distribution

Taking the adopted redshifts in Table 1, the overall median of the 18 primary target SMGs is 3.3 ± 0.3 with a bootstrapping uncertainty that is slightly larger than that of the photometric redshifts (3.1 ± 0.2) simply due to the three outliers whose real redshifts are all higher than their photometric redshifts. Three target SMGs, AS2COS0001.1, AS2COS0002.1, and AS2COS0006.1, have been shown to be part of a $z = 4.6$ coherent megaparsec-scale structure (Mitsuhashi et al. 2021).

The uncertainty for the median caused by the measurement errors is on the order of 3×10^{-4} , which is the standard deviation of a set of 1000 medians, each of which is a result of a set of randomly perturbed redshifts generated according to the measurements. The uncertainty for the median caused by the wrongly assigned line transitions for the SMGs with a single line detection is estimated to be 0.1, which is again the standard deviation of a set of 1000 medians, each of which is a result of a set of redshifts that are generated based on the adopted redshifts but having randomly chosen two SMGs with a single line that are randomly assigned to one transition up or down from the adopted one, providing that the new transition would not allow the coverage of another CO transition within the bandwidth. In summary, the dominant contributor to the uncertainty of the median is the bootstrapping uncertainty, essentially reflecting the sample size and the underlying distribution.

4.2.1. Comparisons with Previous Measurements

Previously, redshift measurements of SMGs have been mostly focused on those with $S_{850/870} \sim 2\text{--}10 \text{ mJy}$ (e.g., Chapman et al. 2005; Ivison et al. 2007; Wardlow et al. 2011; Simpson et al. 2014; Cowie et al. 2017; Stach et al. 2019; Birkin et al. 2021). This is simply a result of the typical survey depth and area, coupled with the shape of the number counts, that maximizes the number of detections in this flux range. The median redshifts deduced differ slightly in different studies, but they generally lie in the range of 2.4–2.6, with an uncertainty of about 0.1–0.2. Together with our results, this hints that brighter SMGs are, on average, located at higher redshifts.

Since these previous studies used various methods to estimate or measure redshifts, they often covered different flux ranges. To better assess the correlation between flux density and redshift in Figure 9, we plot the most recent results from self-similar and well-defined samples, namely ALESS (da Cunha et al. 2015), AS2UDS (Stach et al. 2019), and AS2COSMOS (Simpson et al. 2020; S. Ikarashi et al. in preparation). We investigate the

²¹ For example, S2COS850.0003 is one of the brightest submillimeter sources in the S2COSMOS catalog (Simpson et al. 2019), but it breaks into four constituent SMGs in higher-resolution ALMA maps, all of which have S_{870} below our current flux cut (Simpson et al. 2020).

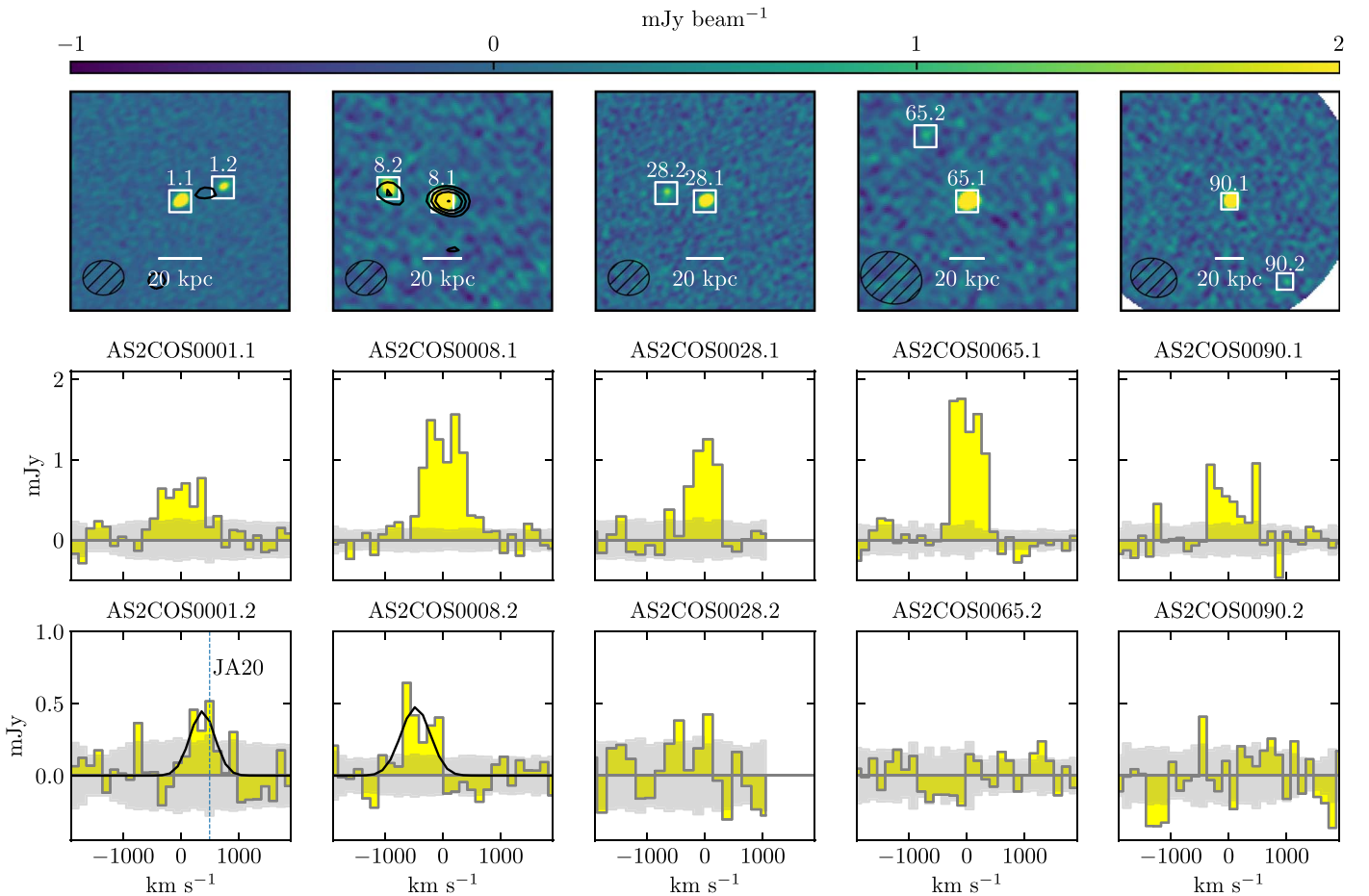


Figure 8. Continuum images at $870\ \mu\text{m}$ and 3 mm spectra of paired SMGs. Top: subarcsecond continuum images at $870\ \mu\text{m}$ from AS2COSMOS (Simpson et al. 2020), with scale bars of 20 kpc marked based on the adopted redshifts in Table 1 for the primary SMGs. The images are uniformly and linearly scaled between -1 and $2\ \text{mJy}$, with a color bar plotted on top. The SMGs are shown by white boxes, and their IDs are indicated. The synthesized beams of the 3 mm spectra adopted for each pair are shown in the bottom left corners, and the black contours are S/N s at 3σ , 4σ , 5σ , and 7σ for the line emissions averaged over the FWHM based on the best-fit single Gaussian model profiles shown in the bottom spectra. Middle and bottom: 3 mm spectra binned to $\sim 150\ \text{km s}^{-1}$ channel $^{-1}$ for the primary (middle panels) and secondary (bottom panels) SMGs. These spectra are extracted using apertures centered on their reported $870\ \mu\text{m}$ locations (Simpson et al. 2020) with the sizes and shapes of their corresponding synthesized beams. The velocities are referenced to the redshifts of the primary SMGs (Table 1), and the 1σ rms levels are plotted in gray. For the secondary SMGs, we obtain significant detection from AS2COS0008.2, marginal detection from AS2COS0001.2, and no detection from AS2COS0028.2, AS2COS0065.2, and AS2COS0090.2. There is no line detection from AS2COS0028.2 in both frequency ranges covering CO(3–2) and CO(4–3), and for demonstration purposes, we only show the range of CO(3–2). The spectra of AS2COS0001.2 and AS2COS0008.2 are fitted with single Gaussian model profiles, and the best fits are plotted as black curves. The same line for AS2COS0001.2 was more significantly detected by Jiménez-Andrade et al. (2020) using deeper NOEMA observations, and the line peak deduced based on their results is shown in dashed blue and marked as JA20.

photometric and spectroscopic redshifts separately. In Figure 9, the photometric redshifts of all three samples are combined and shown as density contours. In both cases, the correlation between flux density and redshift can be observed. Indeed, the Spearman correlation coefficients are 0.3 and 0.4 for photometric and spectroscopic redshifts, respectively, and the p -values are $\lesssim 0.001$. The maximum-likelihood linear fitting yields $z_{\text{median}} = (2.2 \pm 0.3) + (0.09 \pm 0.02) \times S_{870}$ for the sample with spectroscopic redshift, consistent with the best-fit based on photometric redshifts. Our results are also consistent with previous assessments regarding either the general trends or the slope (Ivison et al. 2002; Cowie et al. 2017; Stach et al. 2019; Simpson et al. 2020; Birkin et al. 2021).

Finally, we compare our results to the South Pole Telescope (SPT) SMGs presented by Reuter et al. (2020), where complete measurements of spectroscopic redshifts are reported on a well-defined millimeter-selected SMG sample. The reported SPT SMGs have apparent flux densities of $S_{870} > 25\ \text{mJy}$, and they are mostly strongly lensed. In Figure 9, we show their redshift

distributions with respect to the intrinsic flux densities where gravitational magnifications are accounted for. Interestingly, the distribution of the SPT SMGs appears to follow our unlensed SMGs at $S_{870} \gtrsim 10\ \text{mJy}$, below which the known selection effect of lensing biasing sources toward higher redshifts can be clearly seen.

4.2.2. Comparisons with Models

We now compare our measurements to model predictions. Currently, there are various schools of models that can reproduce basic properties of SMGs, such as number counts, and have made predictions for other properties, such as redshifts. They include empirical models (e.g., Béthermin et al. 2012, 2017; Casey et al. 2018; Zavala et al. 2021); semiempirical models (e.g., Hayward et al. 2013b; Popping et al. 2020); semianalytical models (e.g., Lacey et al. 2016; Lagos et al. 2020); hybrid models, including both analytical and empirical recipes (e.g., Negrello et al. 2007, 2017; Cai et al. 2013); and hydrodynamical simulations with various treatments of dust and its emissions

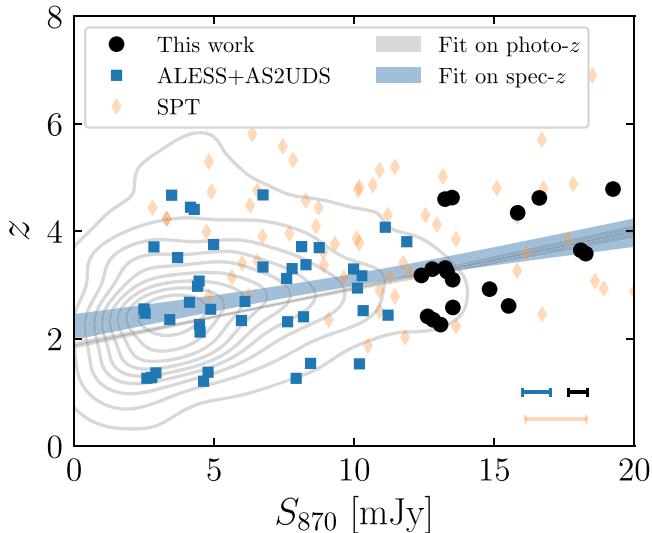


Figure 9. Redshift distribution as a function of S_{870} based on uniformly selected SMG samples with ALMA follow-up observations. The spectroscopic redshifts of this work are plotted with black circles, and those for the ALESS and AS2UDS subsamples are plotted with blue squares, which are reported by Birkin et al. (2021). We also plot the spectroscopic redshifts of the SPT SMGs vs. their intrinsic flux densities (Reuter et al. 2020). Typical uncertainties for the spectroscopic redshift samples are shown at the bottom right corner with matching colors. The background density contours show the distribution of photometric redshifts based on the three samples, ALESS (Simpson et al. 2014), AS2UDS (Stach et al. 2019), and AS2COSMOS (S. Ikarashi et al. in preparation). The results of linear fittings on the photometric and spectroscopic redshifts of the combination of ALESS, AS2UDS, and our results are plotted as gray and blue bands, respectively, where the widths represent 68% confidence levels. The slope of the best-fit model on the spectroscopic redshifts is 0.09 ± 0.02 , consistent with that of photometric redshifts and previous studies (Cowie et al. 2017; Stach et al. 2019; Simpson et al. 2020; Birkin et al. 2021).

(e.g., McAlpine et al. 2019; Hayward et al. 2021; Lovell et al. 2021).

In general, while good progress has been made over the years, it is still difficult to find in hydrodynamical simulations as many bright SMGs as are detected in observations. For example, imposing the flux cut of our sample, there are only two such sources in the model presented by Lovell et al. (2021), and similar or fewer numbers are seen in other hydrodynamical models (McAlpine et al. 2019; Hayward et al. 2021). The lack of SMGs brighter than our flux cut could be due to the fact that current simulations do not have sufficient volumes, which are typically about 100 cMpc on a side. As a result, for a meaningful comparison, we do not consider predictions based on hydrodynamical simulations in this section.

We list the model catalogs used for comparisons and their details in Table 2, including the area from which the catalogs are drawn and the methods used to generate these catalogs. Briefly, all of these models employ certain methods to predict SFRs, and thus total infrared luminosity (L_{IR}), and adopt various templates or relations to model the infrared and submillimeter SEDs. For example, analytical solutions of SFRs are calculated in physically motivated models like SHARK and Cai–Negrello, where the predicted submillimeter flux densities are modeled using selected SED templates. For models like SIDES and Popping, SFRs are estimated by fitting their dark matter base empirical models to stellar mass functions with considerations of the star formation main sequence. SIDES then adopts an SED template to model submillimeter fluxes,

where Popping applies a relation between the 850 μm flux density and SFRs and dust masses based on dust radiative transfer codes. Casey–Zavala obtains L_{IR} directly by modeling the infrared luminosity functions, and a modified blackbody plus mid-infrared power-law SED model was assumed, together with a relation between dust temperature and L_{IR} . The full descriptions of the methodologies used to generate these model catalogs can be found in the latest reference for each model listed in Table 2. However, note that for Cai–Negrello, the model has been slightly updated with a new version of the SED template, resulting in a better agreement with the recently reported number counts in the far-infrared and submillimeter (M. Negrello et al. 2022, in preparation).

We assess their redshift distributions as follows. For SIDES, since it is drawn from an area that has a size similar to our initial SCUBA-2 survey, we simply impose the flux cut of our sample and plot the cumulative distribution in Figure 10. For model catalogs that are drawn from areas that are much larger than 2 deg^2 , we randomly draw the model catalogs 100 times based on the size of our surveyed area. For each draw, we assess the cumulative distribution, and in Figure 10, we plot the median of all 100 draws, as well as their 10th–90th percentile range, to roughly indicate the fluctuations of these distributions, which are mainly due to their field-to-field variations and shot noise.

To compare our observational results to the models, we generate a set of 100 randomly perturbed redshift distributions based on our measurements and their associated uncertainties, as well as the probability of wrongly assigned redshifts for SMGs with only a single line detection, following the procedure described in the previous paragraph. The results are plotted in Figure 10, again with a 10th–90th percentile range. We then perform a two-sample Kolmogorov–Smirnov (K-S) test between each of the 100 perturbed observational distributions and each of those 100 drawn from each of the model catalogs, for a total of 10,000 comparisons, except for SIDES, which only has 100. For each model catalog, we record the p -values of each comparison and compute the percentage of them having $p < 0.05$, a standard value that suggests that the difference between the two samples is highly significant. Changing this p -value cut does not affect the conclusion. We show the results of these comparisons in Figure 10. Strikingly, all models predict lower redshifts compared to our measurements, although from the statistical point of view, the significance of their differences differs. Our measurements agree best with SIDES; however, SIDES only provides one sight line. With a much larger volume, perhaps the comparison against SIDES would yield a result that is similar to that from the comparison against Cai–Negrello. The most significant difference comes from the comparison against SHARK, where all sight lines that we draw do not agree with our measurements.

We can also compare them in median redshifts, which are 1.7 ± 0.3 for SHARK, 2.9 ± 0.7 for SIDES, 2.6 ± 0.3 for Casey–Zavala, 2.1 ± 0.4 for Popping, and 2.9 ± 0.4 for Cai–Negrello. The error budget again includes both statistical and systematic uncertainties caused by field-to-field variations and the shot noise of the simulations. Our measured median redshift of 3.3 ± 0.3 is larger compared to all models, with the least agreement with SHARK, which is in 3.8σ tension. These are the same conclusions we make based on more detailed two-sample K-S tests. Measurements based on a much larger sample size (i.e., a factor of a few more) would allow meaningful tests on the surviving models.

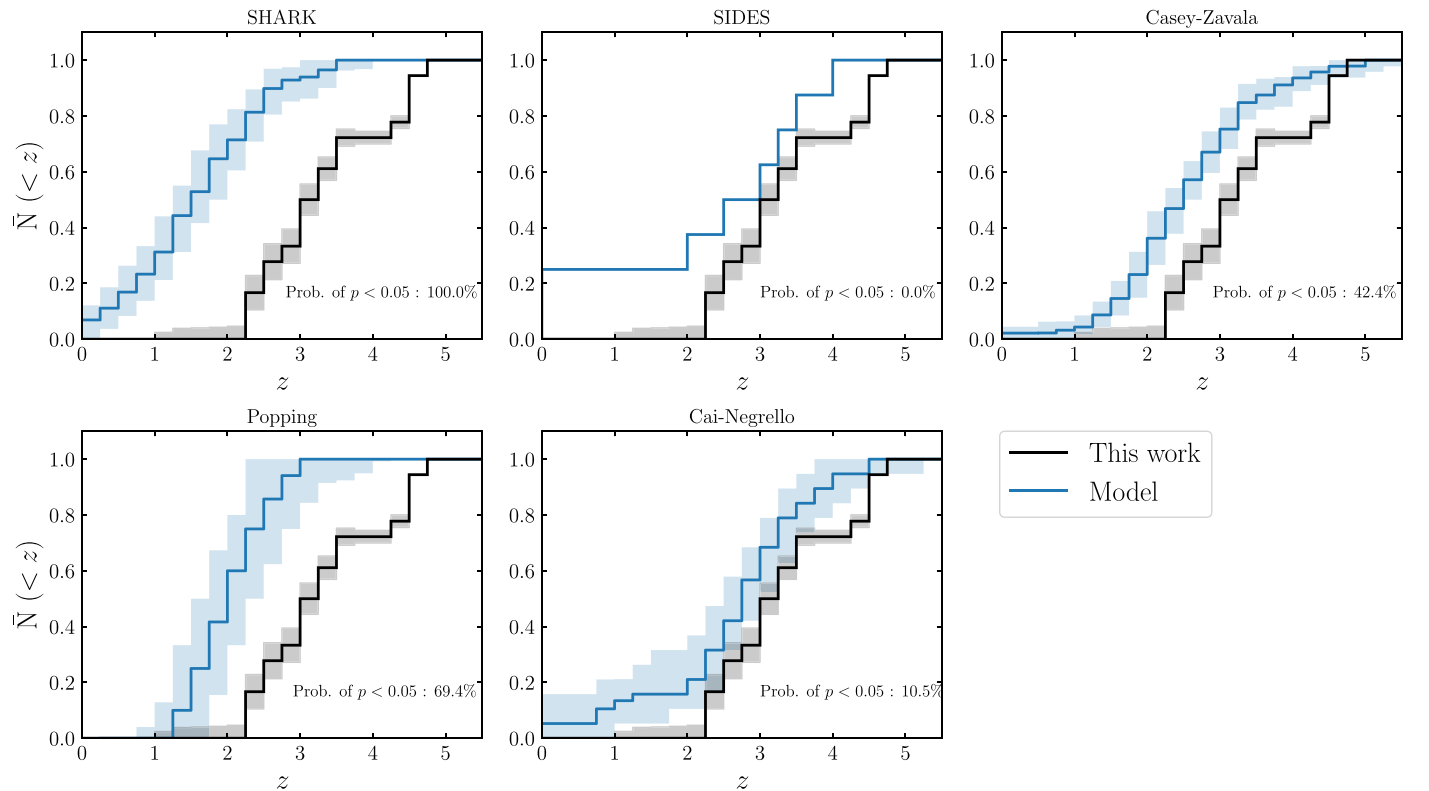


Figure 10. The cumulative distributions of our measured redshifts in are shown in black, and the distributions of each model catalog, summarized in Table 2, are plotted in blue with their associated model names indicated on top. The 10th–90th percentile distributions for each curve are based on simulations described in Section 4.2. In each panel, the probability of finding $p < 0.05$ from a set of two-sample K-S tests based on simulations of the two comparison distributions are shown.

Table 2
Model Catalogs Used for Comparisons

Model	Method	Area [deg ²]	Lensing	References
Cai–Negrello	Analytical + empirical	500	Yes	Cai et al. (2013), Negrello et al. (2017)
SIDES	Empirical	2	Yes	B��thermin et al. (2017)
Casey–Zavala	Empirical	10	No	Casey et al. (2018), Zavala et al. (2021)
Popping	Semiempirical	22.2	No	Popping et al. (2020)
SHARK	Semianalytical	107.9	No	Lagos et al. (2019, 2020)

4.2.3. Implications

The physical reasons for brighter SMGs lying at higher redshifts remain unclear. It is worth noting that among models that are used to compare with our results, SHARK is the only one that is created with a complete suite of physically motivated treatments, including merger trees of cold dark matter and baryon physics. It is also intriguing to note that another self-consistent and physically motivated semianalytical model, GALFORM (Lacey et al. 2016), made with a different treatment of physics, has also predicted a low redshift ($z < 2$) for the flux range of our sample and a negative correlation between $S_{850/870}$ and redshift (Cowley et al. 2015).

Other physically motivated models based on hydrodynamical simulations like EAGLE (McAlpine et al. 2019), Illustris/IllustrisTNG (Hayward et al. 2021), and SIMBA (Lovell et al. 2021) have recently made good progress in matching number counts at the typical flux regime ($\lesssim 10$ mJy). While they are not yet capable of making a significant amount of $\gtrsim 10$ mJy SMGs, in part due to the limited volume, many are successful in reproducing the median redshifts of fainter SMGs, although not all can reproduce the trend between flux density

and redshift (McAlpine et al. 2019). These efforts have pointed to the need to better understand the properties of dust, in particular the relationship between dust, metal, and gas masses, such as the dust-to-metal ratios, in order to address the issue that models tend to underpredict dust masses for SMGs. For example, recent measurements of the dust mass of SMGs have arrived to an average of about $(6\text{--}7) \times 10^8 M_\odot$ (Dudzevi  t   et al. 2020; da Cunha et al. 2021), somewhat higher than what is seen in most models. In a forthcoming paper (C.-L. Liao et al. 2022, in preparation), we will show that our sample SMGs have even higher dust masses. On the other hand, subgrid physics regarding the feedback processes has been suggested to be the key in making enough dust in models (Hayward et al. 2021).

Moving forward, observational constraints on various physical properties would be required to solve the puzzle of the formation of SMGs. For example, measuring dust-to-metal ratios for dusty galaxies through observations would be key in testing the predicted values from recent models. ALMA has been proven invaluable in the measurements of dust and gas masses, as well as dust properties such as the dust emissivity

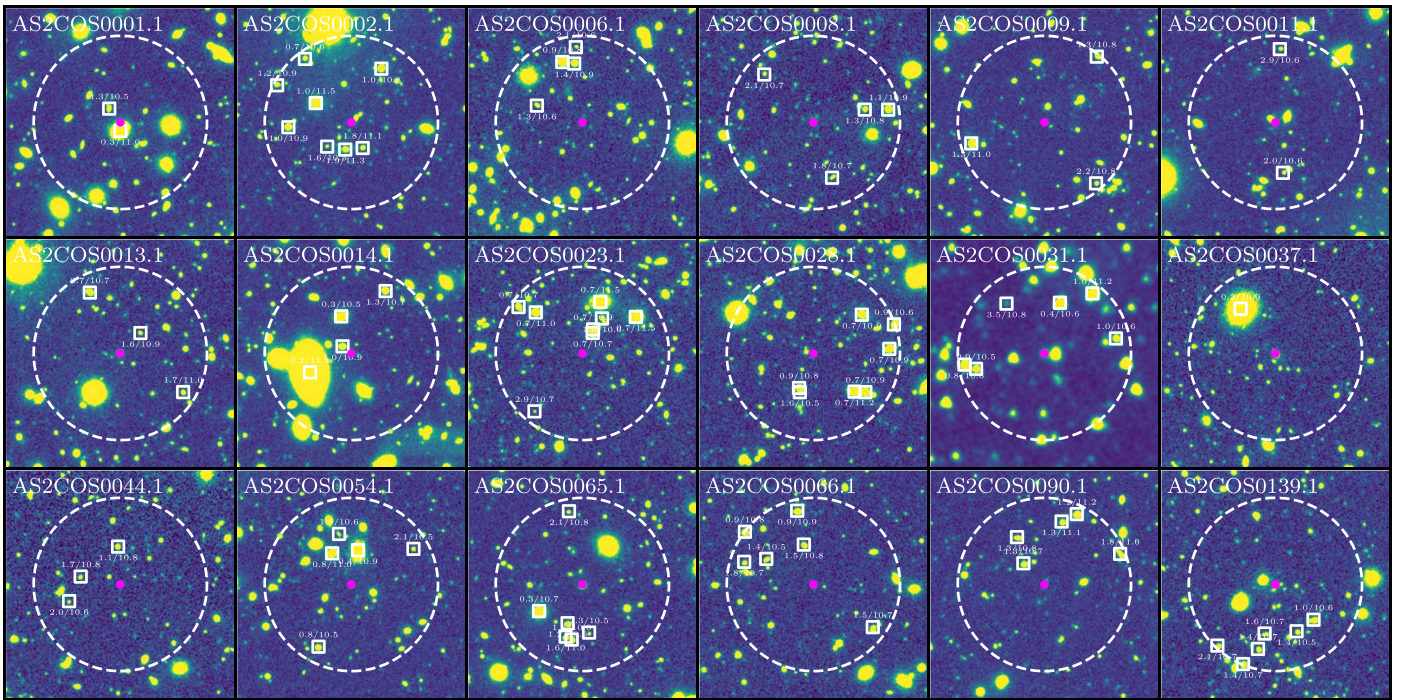


Figure 11. Thumbnail images in the K band ($3.6 \mu\text{m}$ for AS2COS0031.1) of our 18 sample SMGs. The large dashed white circles with a radius of $30''$ and centered on our sample SMGs (magenta points) show the search area for constructing the foreground potential. Small open squares mark the neighboring foreground galaxies that have stellar masses $>10^{10.5} M_{\odot}$. The corresponding small values for each box are redshift on the left and stellar mass in logarithm base 10 on the right.

index and temperature. Measurement of gas-phase metallicity, on the other hand, has been a challenging task for dusty galaxies due to them often being faint in the rest-frame optical. One can always start with those that are significantly detected on the optical strong emission lines, although one needs to also bear in mind the largest possible biases toward the galaxies that may have the largest spatial offsets between dust and optical emissions or the subset that is the least obscured. Far-infrared fine-structure lines from [N II] and [O III] offer a promising way to measure the gas-phase metallicity of dusty galaxies (e.g., Rigopoulou et al. 2018), but a future facility, such as a sensitive far-infrared probe satellite, would be required to conduct such measurements on a large sample at cosmic noon. Finally, upcoming facilities such as the James Webb Space Telescope could provide subkiloparsec rest-frame near-infrared imaging, which would help constrain stellar mass and morphology, addressing the issue of the triggering of star formation, which has also been a topic of debate.

4.3. Gravitational Lensing

Strong gravitational lensing (lensing magnification $\mu > 2$) is found to be responsible for the exceptional apparent brightness ($S_{500 \mu\text{m}} \gtrsim 100$, $S_{1.4 \text{mm}} \gtrsim 10$, or $S_{850 \mu\text{m}} \gtrsim 30$ mJy) of the majority of the submillimeter and millimeter sources that are uncovered by shallow but wide surveys such as those conducted by the SPT and Herschel (Negrello et al. 2010, 2017; Bussmann et al. 2013; Hezaveh et al. 2013; Wardlow et al. 2013; Spilker et al. 2016). Most models predict that the fraction of sources experiencing strong lensing drops significantly, from about $\gtrsim 70\%$ to almost zero, within a narrow range of flux density, which is about 80–100 mJy at $500 \mu\text{m}$ and 10–30 mJy at $850 \mu\text{m}$ (Wardlow et al. 2013; Negrello et al. 2017). Our statistical sample SMGs have their flux densities within this

range and therefore represent an opportunity to test model predictions.

To estimate the lensing magnifications of our sample SMGs, we employ LENSTOOL (Kneib et al. 1996; Jullo & Kneib 2009). For each SMG, we utilize the COSMOS15 catalog (Laigle et al. 2016) and construct a list of neighboring galaxies that are located within $30''$ of the SMG and have had reported estimates of photometric redshifts and stellar masses. This angular distance is chosen because beyond it, the results do not change significantly. A gallery of the selected massive subsets of these neighboring galaxies is plotted for each SMG in Figure 11. To construct a model of the foreground gravitational potential for each SMG, we assume a regular Navarro–Frenk–White (NFW) density profile ($\alpha = 1$; Navarro et al. 1997) for each neighboring galaxy in the list. Besides sky position, other key input parameters for the model of each neighboring galaxy include ellipticity, position angle, scale radius r_s , and characteristic velocity σ_s (Limousin et al. 2005). We describe the procedures for obtaining these parameters in the following.

We first run SEXTRACTOR (Bertin & Arnouts 1996) to obtain the structural parameters ellipticity and position angle, and the primary image considered is the K -band image from UltraVista DR4, except for AS2COS0031.1, where it is outside the UltraVista footprint, so we adopt the $3.6 \mu\text{m}$ image from Spitzer. The scale radius and characteristic velocity are related to the assumed NFW profile, which is expressed as

$$\rho(r) = \frac{\rho_s}{(r/r_s)(1 + r/r_s)^2},$$

where r_s is the scale radius and ρ_s is the characteristic density so that the characteristic velocity is $\sigma_s = 4/3 G r_s^2 \rho_s$. Here ρ_s can be related to critical density ρ_c as $\rho_s = \delta_c \rho_c$, where the density contrast $\delta_c = 200c^3 / (3 \ln(1 + c) - 3(c/1 + c))$, and c is the

Table 3
Lensing Magnifications

ID	μ
AS2COS0001.1	$1.4^{+0.1}_{-0.1}$
AS2COS0002.1	$3.0^{+1.4}_{-0.7}$
AS2COS0006.1	1.1
AS2COS0008.1	1.1
AS2COS0009.1	1.0
AS2COS0011.1	1.1
AS2COS0013.1	1.1
AS2COS0014.1	$1.7^{+0.5}_{-0.2}$
AS2COS0023.1	$1.7^{+0.1}_{-0.1}$
AS2COS0028.1	1.1
AS2COS0031.1	1.1
AS2COS0037.1	1.1
AS2COS0044.1	1.1
AS2COS0054.1	1.1
AS2COS0065.1	1.0
AS2COS0066.1	1.1
AS2COS0090.1	1.1
AS2COS0139.1	1.1

Note. Details can be found in Section 4.3. Uncertainties less than 0.05 are omitted.

concentration factor defined as the ratio between the halo radius r_{200} (the mean density within which is $200\rho_c$) and r_s . The halo mass can therefore be deduced as $M_{200} = 800/3\pi r_{200}^3 \rho_c$. That is, r_s and σ_s can be derived for a given combination of concentration factor and halo mass.

For each neighboring galaxy, we estimate its halo mass by adopting the stellar mass and redshift provided by the COSMOS15 catalog and applying the latest stellar-to-halo mass relationships given by Legrand et al. (2019). For concentration, we refer to the classical work of Wechsler et al. (2002) based on dark matter N -body simulations of Λ CDM cosmology, where the relationships between concentration, halo mass, and redshift are shown.

Each of the adopted input parameters has its own reported uncertainty or scatter, and they should be taken into account in order to properly assess the probability distributions of lensing magnifications. To do so, for each SMG, we create 100 potential models, where each constituent potential is created by randomly perturbing each of their parameters based on their quoted uncertainties. We run LENSTOOL on these 100 potential models for each SMG and calculate the median and 1σ percentile. The results are given in Table 3.

As a check, the lensing magnification of AS2COS0001.1 was also estimated by Jiménez-Andrade et al. (2020) with a different assumption of the density profile, and they found a factor of 1.5, consistent with our results. Notably, we find that if we only look at the mass distributions of much closer surroundings, the magnifications of a few SMGs, such as AS2COS0002.1 and AS2COS0014.1, would be significantly underestimated. This is because in these cases, there are a few very massive (up to $10^{11.5} M_\odot$) foreground galaxies, and in the case of AS2COS0002.1, a number of galaxies, including the very massive ones, are located at $z \sim 1$, suggesting a group environment.

Based on Table 3, we can see by looking at their medians that only one out of the 18 SMGs in our sample can be classified as being strongly lensed with $\mu > 2$, suggesting a relatively low strongly lensed fraction of $<10\%$ compared with

the brighter sources. This is in line with what has been predicted by some observations (Chapman et al. 2002) and models. We note that our methodology in constructing foreground gravitational potentials does not account for contributions from halos larger than galactic halos (i.e., group-scale halos); thus, it is possible that the magnifications of some SMGs may have been underestimated by a moderate amount. On the other hand, our methodology also does not account for underdense regions, so the overall magnification is slightly biased high, and as a result, many unlensed SMGs have $\mu = 1.1$. Nevertheless, these two factors are not expected to affect our results significantly.

We compare our results with predictions of magnification for the flux range of our sample from SIDES and Cai–Negrello in Figure 12 and find that our results are inconsistent with SIDES but consistent with Cai–Negrello. This can be understood by the fact that, while the Cai–Negrello model takes into account both the redshift distribution of model SMGs and the mass distributions in the foreground, the predictions from SIDES are simply drawn from some probability distributions according to the redshifts of the model SMGs, as stated in Béthermin et al. (2017).

We now expand the comparisons by including published measurements for a wide range of $870 \mu\text{m}$ flux densities, including the Submillimeter Array (SMA) and ALMA follow-up studies of Herschel-selected sources (Bussmann et al. 2013, 2015), as well as those based on the SPT survey (Spilker et al. 2016). For each of the SPT sources, separate magnification factors were reported for each of their constituent components, so we compute their flux-weighted magnification as the nominal magnification for each SPT source (Figure 3 in Spilker et al. 2016). It is also worth noting that while the Herschel-selected sample observed by the SMA is a flux-limited sample, the one observed by ALMA was selected to have a nearby foreground source to maximize the probability of detecting strongly lensed objects. As a result, the Herschel-selected sample observed by ALMA is likely biased high in lensing magnification for the same flux range.

The results are plotted in Figure 13, where we find that despite the possibility of having a bias, the Herschel–ALMA measurements are consistent with our results at the overlapping flux density range (10–20 mJy). We can also compare to the model predictions from Cai–Negrello. Note that in the Cai–Negrello model, sources that are not strongly lensed ($\mu < 2$) are assigned 1 for their magnification. We therefore adopt the same method for the measurements and compute the binned median with bootstrapped errors. We compare our results with the median of the model prediction with the same flux bins and find that they have good agreement overall.

Last but not least, having lensing magnification measurements of a flux-limited sample means that we can compute the number counts of the strongly lensed SMGs. The cumulative number counts of the parent AS2COSMOS sample were presented in Simpson et al. (2020), and they are plotted in Figure 14. Since our sample is limited to 12.4 mJy at $870 \mu\text{m}$, the cumulative counts for the strongly lensed SMGs can be simply scaled from the parent counts of the corresponding flux bin (12.1 mJy in this case) by dividing its value by our sample size. There is no source between 12.1 and 12.4 mJy, so no correction needs to be applied. To estimate the uncertainty, the Poisson error of 1 is adopted and propagated based on the uncertainty of the parent counts. The results are shown in Figure 14 as the red point. As a check, the value is very close to one divided by the size of the

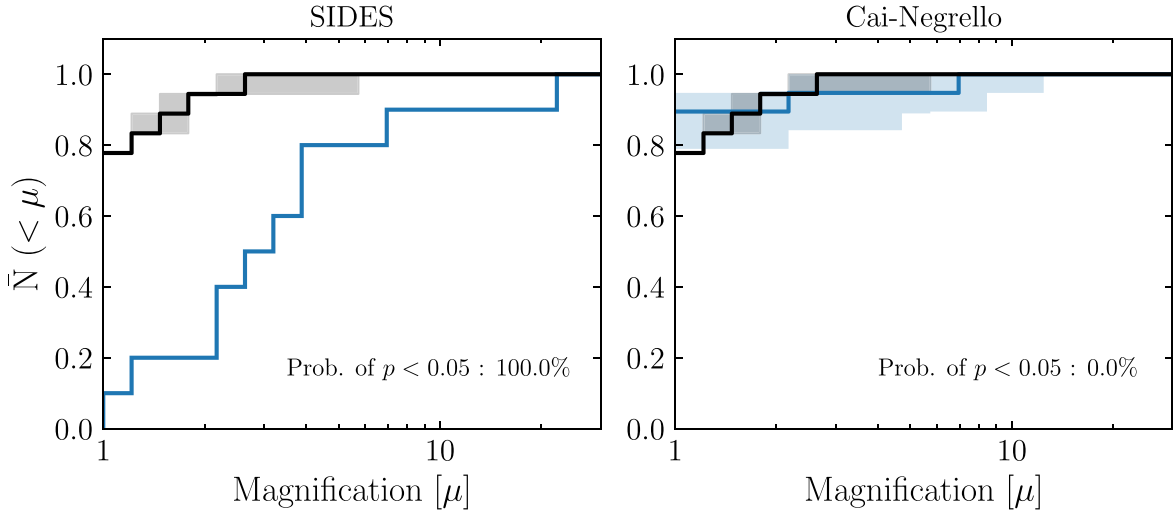


Figure 12. Cumulative distributions of estimated lensing magnifications in black and those based on model predictions of SIDES and Cai–Negrello in blue, with the corresponding model names indicated on top. The 10th–90th percentile distributions for each curve are based on simulations done in a similar fashion as described in Section 4.2. In each panel, the probability of finding $p < 0.05$ from a set of two-sample K-S tests based on simulations of the two comparison distributions is shown.

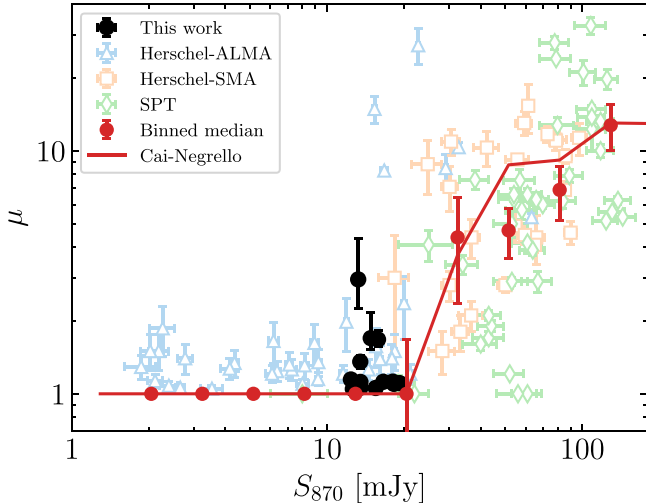


Figure 13. Lensing magnification as a function of $870 \mu\text{m}$ flux density. The estimates for our sample SMGs are shown with black circles, and various estimates from other studies are plotted with different symbols, including blue triangles for an ALMA study of Herschel-selected sources (Bussmann et al. 2015), orange squares for an SMA study of a brighter Herschel-selected sample (Bussmann et al. 2013), and green diamonds for the results from the SPT survey (Spilker et al. 2016). The red circles are binned medians where magnifications of $\mu < 2$ are assigned to 1, following the method that is used to generate the model catalog by Cai–Negrello (Negrello et al. 2007; Cai et al. 2013), which is shown as the red curve. Overall, we find that the measurements are consistent with model predictions across this 2 orders of magnitude flux range.

footprint of the primary S2COSMOS catalog, so one divided by 1.6 deg^2 . Overall, we again find good agreement with the model prediction of Cai–Negrello.

4.4. Connecting to the Descendants

As shown in Section 3.2, we find that the emission lines of 15 out of the 17 ($\sim 90\% \pm 30\%$) primary SMGs with line detections appear to be better modeled by double Gaussian profiles. This high fraction of SMGs exhibiting double Gaussian line profiles is in contrast with previous studies of other SMGs samples, which have typically reported fractions under 50% (Greve et al. 2005; Bothwell et al. 2013;

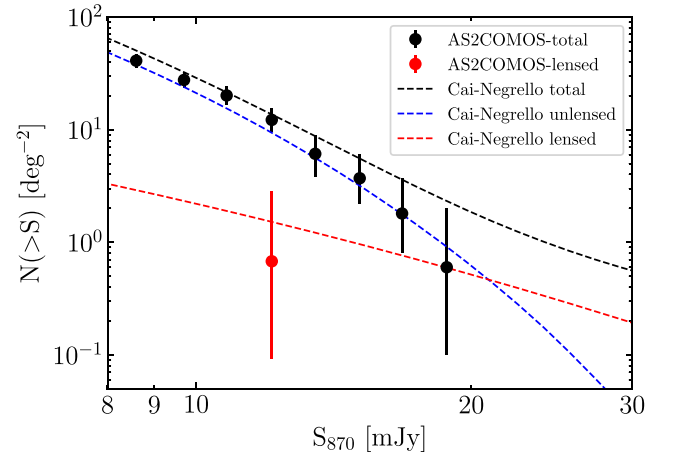


Figure 14. The cumulative number counts of the parent AS2COSMOS sample are plotted with black circles, and the counts of strongly lensed ($\mu > 2$) SMGs are shown with a red circle, which is scaled from the counts of the parent sample with a factor of $1/18$, the strongly lensed fraction based on Table 3. The count predictions based on the Cai–Negrello model are plotted in black for total counts, blue for no strongly lensed counts, and red for strongly lensed counts.

Birkin et al. 2021). This could be in part due to our smaller sample size, or it could be because of our sample SMGs being brighter so that they may appear dynamically distinct from their fainter counterparts. Unless dispersion-dominated, it is expected that the lines would appear as double Gaussian in systems that exhibit velocity gradients due to either orderly rotating disks or mergers. Spatially resolved dynamical studies are needed to make a more definite conclusion on their physical origins.

On the other hand, we find that in our sample, for lines that are better described by a double Gaussian, the median separation in velocity between the red and blue peaks is $430 \pm 40 \text{ km s}^{-1}$, which is consistent with previous studies using their double-peaked SMGs (Bothwell et al. 2013; Birkin et al. 2021), as well as recent spatially resolved observations of CO/[C II] lines on a few SMGs (Chen et al. 2017; Calistro Rivera et al. 2018; Litke et al. 2019). This measurement of red and blue velocity separations allow us to crudely estimate dynamical masses, provided there are some reasonable

assumptions. The dynamical mass estimate can be expressed as $M_{\text{dyn}} = C(v_c/\sin(i))^2 \times R/G$, where G is the gravitational constant, v_c is the circular velocity, R is the representative radius, C is the correction factor depending on the mass distributions and the adopted representative radius, and i is the inclination angle. This assumes a rotation-dominated system, which is supported by recent high-resolution and high-sensitivity dynamical measurements of SMGs (e.g., De Breuck et al. 2014; Lelli et al. 2021; Rizzo et al. 2021). Assuming an exponential disk profile with a scale length h and a half-light radius r_e , it has been shown that $R = 3h = 1.79r_e$ ²² is a good approximation for spatially unresolved CO observations (de Blok & Walter 2014). Under this assumption of an exponential disk, C is about 2 (Binney & Tremaine 2008). We adopt $r_e = 3$ kpc based on recent spatially resolved CO measurements of SMGs (Chen et al. 2017; Calistro Rivera et al. 2018), and v_c is half of the median velocity separation that we measure. Since v_c in our case is an average over a sample of sources with random inclination angles, we adopt an average $\langle \sin^2(i) \rangle = 2/3$ (Tacconi et al. 2008). Since the dynamical mass estimated this way only includes mass within the assumed r_e , we multiply by a factor of 2 to obtain the total dynamical mass. As a result, we estimate a total dynamical mass of $M_{\text{dyn}} = 3.5 \pm 0.6 \times 10^{11} M_{\odot}$. Accounting for the typical dark matter fraction at high redshifts, which was recently reported as 12% by Genzel et al. (2020), we deduce a total baryon mass of $M_{\text{baryon}} = 3.1 \pm 0.6 \times 10^{11} M_{\odot}$. Note that the observational constraints on the dark matter fraction are obtained from galaxies at $z \sim 2$, slightly lower than our sample SMGs. However, recent IllustrisTNG hydrodynamical simulations have shown that the dark matter fractions are expected to be lower at higher redshifts (Lovell et al. 2018). On the other hand, the simulations have predicted about a factor of 2 higher fractions than those obtained from observations. It is outside the scope of this paper to argue which is correct, although, by adopting either a factor of 2 higher dark matter fraction or no dark matter, our conclusions would not be significantly altered. Finally, in a follow-up paper, where we plan to present the properties of the ISM via CO/[C I] and dust SED measurement and modeling (C.-L. Liao et al. 2022, in preparation), we will show that by including stellar, gas, and dust mass, the average total baryon mass is consistent with the dynamical estimates presented in this work.

Following Birkin et al. (2021), the estimates of total baryon mass and measurements of velocity dispersion via molecular lines allow us to assess the connection between our sample SMGs and their proposed descendants at lower redshifts, such as compact quiescent galaxies at similar redshifts or local massive early-type galaxies (ETGs; Lilly et al. 1999; Swinbank et al. 2006; Alexander & Hickox 2012; Toft et al. 2014; Dudzevičiūtė et al. 2020). This is under the assumption that the total mass and dynamical energy are mostly preserved along the evolution.

In Figure 15, we plot our sample as a combined median, where σ is the median of all of the line moment measurements presented in Section 3.2, which is $260 \pm 21 \text{ km s}^{-1}$. As a comparison, measurements of local ETGs that are based on the MASSIVE (Davis et al. 2019) and ATLAS^{3D} (Cappellari et al. 2013) surveys are shown, as well as the quiescent galaxies ($D_n4000 > 1.55$; Kauffmann et al. 2003; Wu et al. 2018) at $z = 0.6\text{--}1.0$ based on the LEGA-C survey (van der Wel

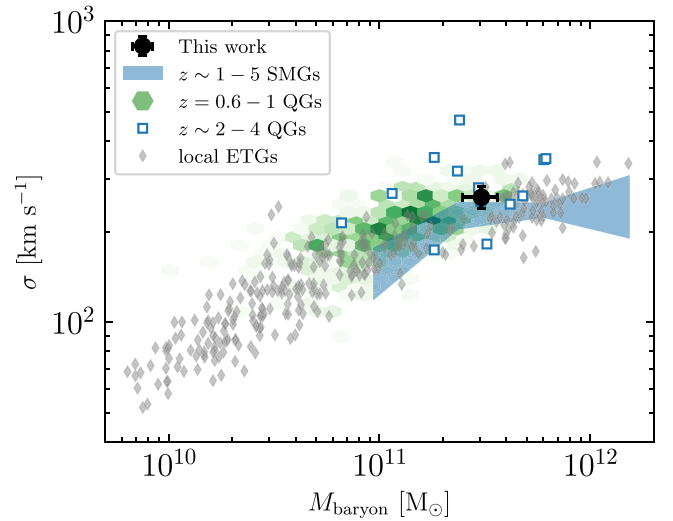


Figure 15. Correlations between baryon mass (M_{baryon}) and velocity dispersion (σ). An overall median is shown by a black circle for both parameters for our sample SMGs. A compiled sample of local ETGs, including MASSIVE (Davis et al. 2019) and ATLAS^{3D} (Cappellari et al. 2013), is plotted in gray, and recent measurements of $z = 0.6\text{--}1.0$ and $z \sim 2\text{--}4$ quiescent galaxies (QGs) are shown as 2D histogram with green hexagon bins (van der Wel et al. 2021; Wu et al. 2021) and blue squares (Stockmann et al. 2020; Valentino et al. 2020), respectively. We also include results of fainter SMGs that also have spectroscopic redshift measurements (Birkin et al. 2021). Our results are consistent with these plotted samples, corroborating the hypothesis that these populations are linked in evolution.

et al. 2021; Wu et al. 2021) and some compiled $z \sim 2\text{--}4$ spectroscopically confirmed quiescent galaxies (Stockmann et al. 2020; Valentino et al. 2020). The results from the similar analyses of mostly fainter SMGs presented by Birkin et al. (2021) are also shown. For ETGs and high-redshift quiescent galaxies, we adopt their stellar masses for the total baryon masses, given that stellar mass dominates baryon mass in these populations, whereas for fainter SMGs in Birkin et al. (2021), stellar, gas, and dust masses are summed to deduce their baryon masses. Our sample of bright SMGs lies in the regions occupied by local ETGs and high-redshift quiescent galaxies, corroborating the proposed evolutionary link among these populations.

In addition, given that our sample is well defined in both flux density and area, we can compute the number densities of our sample SMGs and compare the results with those based on recently confirmed quiescent galaxies at similar redshifts, especially those at $z > 4$. The total number of primary SMGs in the redshift bins of $2.1 < z < 3$, $3 < z < 4$, and $4 < z < 5.1$ is 6, 6, and 5, respectively. The lower bound of the lowest redshift bin is determined by the upper bound of the redshift gap (Section 3.3), and the upper bound of the highest redshift bin is justified by the fact that, given our wavelength coverage, emission lines should have been detected from sources at $z = 5.1\text{--}7.2$. The sky area covered by our initial SCUBA-2 survey is 1.6 deg^2 (Simpson et al. 2019), so the volumes covered in the three redshift bins are all approximately $2.0 \times 10^7 \text{ cMpc}^3$. Thus, the observed number density of SMGs with $S_{870} > 12.4 \text{ mJy}$ is about $3 \times 10^{-7} \text{ cMpc}^{-3}$ for all three redshift bins. However, assuming a typical lifetime of 100 Myr for our sample SMGs (C.-L. Liao et al. 2022, in preparation), the duty cycle corrected number densities are $3.3^{+2.8}_{-1.8} \times 10^{-6}$, $1.9^{+1.6}_{-1.1} \times 10^{-6}$, and $1.0^{+0.9}_{-0.6} \times 10^{-6} \text{ cMpc}^{-3}$ for the three redshift bins, respectively. The uncertainties include Poisson

²² $r_e = 1.68h$ for an exponential disk profile (Chen et al. 2015).

errors and a 40% field-to-field variation (Simpson et al. 2020). Our number density estimate at $z > 4$ is similar to that presented by searches based on Herschel (Ivison et al. 2016) and the ALMA 2 mm survey (Manning et al. 2022), although the sample selections are different and thus direct comparisons are not straightforward.

There has been an active discussion regarding the progenitors of the recently confirmed $z \sim 3-4$ quiescent galaxies, and extreme dusty star-forming galaxies such as SMGs at $z > 4$ have been proposed to be ideal candidates, given their nature (e.g., Straatman et al. 2014; Valentino et al. 2020). From the number density, our results at $z > 4$ appear to be in agreement with those of the $z \sim 3-4$ quiescent galaxies estimated by Davidzon et al. (2017) and Girelli et al. (2019; $\sim 10^{-6}$ cMpc $^{-3}$) but lower by a factor of a few to 10 compared to other estimates ($\sim 10^{-5}$ cMpc $^{-3}$; Straatman et al. 2014; Schreiber et al. 2018; Merlin et al. 2019). The different number densities estimated for quiescent galaxies could be due to selection effects, such as different mass limits, as well as the methods to classify quiescent galaxies. However, given that we are selecting the brightest SMGs, we expect our number density estimates to be lower limits, and fainter SMGs at $z > 4$ are confirmed to exist (Section 4.2.1). We can conclude that our sample of SMGs has the properties expected for the progenitors of some $z \sim 3-4$ quiescent galaxies, especially the most massive ones, with stellar masses of $> 10^{11} M_{\odot}$.

5. Summary

We report the first results of the AS2COSPEC survey, a millimeter spectroscopic survey using ALMA to target the brightest SMGs drawn from AS2COSMOS (Simpson et al. 2020), a sample constructed through ALMA follow-up continuum observations of a flux-limited ($S_{850} > 6.2$ mJy) sample of submillimeter sources uncovered by the single-dish S2COSMOS survey (Simpson et al. 2019). We targeted the brightest 18 primary SMGs with flux densities between 12.4 and 19.3 mJy at 870 μm ($L_{\text{IR}} \sim 10^{13} L_{\odot}$; C.-L. Liao et al. 2022, in preparation), along with five fainter companion SMGs that are located within the primary beam of our observations. The 18 primary SMGs represent a 100% complete selection considering both the original SCUBA-2 and the follow-up ALMA observations. Our findings are as follows.

1. With about 1 hr of observations per target, we detect emission lines in CO or [C I] on 17 of the 18 primary SMGs. This high efficacy ($> 90\%$) represents a major step forward in measuring the spectroscopic redshifts of high-redshift luminous ($L_{\text{IR}} > 10^{12} L_{\odot}$) dusty galaxies that are otherwise difficult to obtain from traditional OIR spectrographs of 8–10 m class telescopes.
2. Among the five companion SMGs, we obtain a significant line detection from one, AS2COS0008.2. Together with the previously reported line detection toward AS2COS0001.2, we find that the velocity differences of these two pairs are both within 500 km s^{-1} at the projected distance of 20–30 kpc, suggesting that they are gravitationally bound systems and therefore confirmed physically associated pairs. Our results suggest that for SMGs with $S_{870} > 12.4$ mJy, the brightest companion SMGs are physically associated with their corresponding primary SMGs $\geq 40\%$ of the time, suggesting that mergers play a role in the triggering of star formation in these exceptional sources.

3. The overall median redshift of the 18 primary SMGs is 3.3 ± 0.3 , confirming that brighter SMGs are located at higher redshifts. By carefully comparing with various model predictions, we find that although the significance differs, our measured redshift distribution is higher than the predictions of those models, where the only model made with a complete suite of physically motivated treatments has the most significant disagreement, at 3.8σ . We suspect that this may be because the models lack halos with sufficiently massive gas reservoirs, which may be caused by either too efficient star formation or too much feedback at even earlier times.
4. By exploiting the rich ancillary data sets in the COSMOS field, we carefully model the foreground gravitational fields and find that only one of the 18 primary SMGs can be strongly lensed with a magnification $\mu > 2$, suggesting a strongly lensed fraction of $< 10\%$. Our results are consistent with previous studies focusing on Herschel-selected dusty galaxies, as well as the empirical model that interprets SMGs as protospheroidal galaxies.
5. With these high-S/N spectra, we determine that about 90% of the primary SMGs have their emission lines better described with double Gaussian profiles. The median separation of the two line peaks of the best-fit double Gaussian models is $430 \pm 40 \text{ km s}^{-1}$, consistent with previous studies, where redshifted and blueshifted components are spatially resolved. The average dynamical mass ($3.5 \pm 0.6 \times 10^{11} M_{\odot}$) estimated based on the velocity separation, together with the median line dispersion measured, puts our primary SMGs on similar mass- σ correlations found on local ETGs and high-redshift quiescent galaxies, corroborating the proposed evolutionary link among these populations.
6. Lastly, given the well-defined nature of our sample, we estimate that the number density of our primary SMGs at $z = 4-5.1$ is $1_{-0.6}^{+0.9} \times 10^{-6}$ cMpc $^{-3}$ after accounting for the duty cycle, for which we assume a typical lifetime of 100 Myr. This suggests that our primary SMGs can be the progenitors of some $z \sim 3-4$ quiescent galaxies, especially the most massive ones ($> 10^{11} M_{\odot}$).

We demonstrate the power of millimeter spectroscopic redshift surveys on a complete sample of bright SMGs in constraining theoretical models. In a forthcoming paper (C.-L. Liao et al. 2022, in preparation), we will present the detailed analyses of the ISM properties of this sample of $z \sim 3$ HyLIRGs ($L_{\text{IR}} \gtrsim 10^{13} L_{\odot}$). These efforts are in line with future developments of ALMA, ngVLA, and AtLAST (Geach et al. 2019; Klaassen et al. 2020), where submillimeter and millimeter spectroscopic surveys are expected to bring fundamental breakthroughs to our understanding of high-redshift, dust-enshrouded galaxies.

We thank the reviewer for a constructive report that improved the manuscript. We would also like to thank Mathieu Bethermin, Caitlin Casey, Chris Hayward, Claudia Lagos, Chris Lovell, Mattia Negrello, Gergo Popping, Martin Sparre, and Jorge Zavala for sharing their catalogs and thoughts about their models. We also thank Hsi-Wei Yen for the suggestions on the automasking approach and Po-Feng Wu for sharing the stellar mass estimates of the LEGA-C sample. C.C. acknowledges support from the Ministry of Science and Technology of Taiwan (MOST 109-2112-M-001-016-MY3).

I.R.S. and A.M.S. acknowledge support from STFC (ST/T000244/1). H.U. is supported by JSPS KAKENHI grant No. 20H01953. A.J.B. acknowledges funding from the ‘‘First-Galaxies’’ Advanced Grant from the European Research Council (ERC) under the European Union’s Horizon 2020 research and innovation program (grant agreement No. 789056). The Cosmic Dawn Center (DAWN) is funded by the Danish National Research Foundation under grant No. 140. This paper makes use of the following ALMA data: ADS/JAO.ALMA#2019.1.01600.S. ALMA is a partnership of ESO (representing its member states), NSF (USA) and NINS (Japan), together with NRC (Canada), MOST and ASIAA (Taiwan), and KASI (Republic of Korea), in cooperation with the Republic of Chile. The Joint ALMA Observatory is operated by ESO, AUI/NRAO and NAOJ.

Facility: ALMA.

Software: astropy (Astropy Collaboration et al. 2013), CASA (McMullin et al. 2007).

Appendix A Spectral Line Model Fitting

To understand which model, single or double Gaussian, better describes the spectra, we employ the BIC and AICc, defined as

$$\begin{aligned} \text{BIC} &= k \ln(n) - 2 \ln(\hat{L}), \\ \text{AICc} &= 2k + \frac{2k^2 + 2k}{n - k - 1} - 2 \ln(\hat{L}), \end{aligned}$$

where k is the number of parameters in the model, and n is the number of data points. Here \hat{L} represents the maximized value of the likelihood function of the model, and in our case, it is simply $\hat{L} = \exp^{-\chi^2/2}$, where χ^2 is the minimized χ^2 value derived from the fitting. Note that when $n \rightarrow \infty$, AICc becomes the original definition of AIC. In both cases, whichever model produces a lower value is expected to be closer to the truth. However, each has its own limitations; in particular, BIC typically imposes a heavier penalty on additional parameters, so it tends to be more conservative. Circumstances thus need to be considered to select the most optimal model. Our strategy is to make the selection based on the results of both criteria in combination with probability estimates from a set of Monte Carlo simulations.

The procedure is detailed as follows. All of the measured spectra are first fit by both single and double Gaussian models.²³ The resulting reduced χ^2 and the preferred model based on the two information criteria are presented in Table A1. For each line, the two best-fit models are then used to create two respective sets of mock spectra, where each set contains 500 mock spectra made by adding the corresponding

best-fit model to the noise spectra drawn from 500 random positions. Each noise spectrum has the same frequency range as the measured spectrum, so this method has the advantage of preserving the noise structures, and thus the weights for fitting, in the frequency domain (Figure 2). Each mock spectrum is then fit by both single and double Gaussian models with exactly the same settings as are used to fit the measured spectra, and the selection of the preferred model is then performed and recorded. Finally, we estimate the probability of a given line being better described by a single or double Gaussian model by doing the following. First, we select the mock spectra that have preferred models matched to those of the measured spectrum, and among these selected mocks, we compute the respective fractions of them made with the best-fit single or double Gaussian model. The two fractions computed this way are then the probability estimates of a given line being truly a single or double Gaussian line, and the results are shown in Table A1 in the columns labeled SGprob and DGprob. Note that these probabilities can change in different runs of simulations, but the variation is typically a few percent.

For each line, our final selection of the preferred model then goes to the one that has a higher probability, except for AS2COS0001.1, AS2COS0023.1, and AS2COS0028.1, where our simulations yield inconclusive results due to either the comparable probabilities or conflicting results from the two lines on the same target. Jiménez-Andrade et al. (2020) reported CO(5–4) and [C II] detection on AS2COS0001.1, and, with better S/N measurements, they favored double-peak line profiles for both lines. We therefore adopt their results. For AS2COS0023.1, the single Gaussian model is clearly preferred for CO(5–4). While the double Gaussian model is preferred for CO(4–3), the bluer and fainter component is only marginally detected, with a velocity-integrated significance of $\sim 2\sigma$ over the line FWHM (Figure 6). We therefore adopt a single Gaussian for AS2COS0023.1. Finally, for AS2COS0028.1, although our simulations yield inconclusive results for both CO lines, the fact that the best-fit double Gaussian models have significantly different components suggests that the best fits are unavoidably subject to noise structures, especially for CO(4–3)²⁴ (Figure 6). Given their acceptable χ^2 , we therefore adopt single Gaussian models for AS2COS0028.1 for their consistency and simplicity.

As a check, we perform simultaneous fitting on SMGs that have two lines detected in our data. In this exercise, each source has its redshift fixed for the two lines, and for the double Gaussian models, the velocity separations of the two constituent Gaussians are also fixed. We find that the results are consistent with our decisions. The final selected models are given in the last column of Table A1, and they are further discussed in Section 4.4.

²³ To ensure sensible results, we impose a few loose boundaries. For each Gaussian component, the peak has to be larger than 1σ , and the line widths need to be at least 100 km s^{-1} . The separation of the two peaks for the double Gaussian models should be less than 1000 km s^{-1} . As seen in Figure 6, these limits have a negligible impact on most sources but in a few cases can help avoid fitting to noise peaks.

²⁴ We have tried changing the boundaries for CO(4–3), but the broad component nevertheless appears to be in favor. It would result in a significantly inconsistent second moment between the two lines, which is unlikely to be real.

Table A1
Best-fit Model Selection Based on AICc and BIC

ID	χ^2_{SG}	χ^2_{DG}	AICc	BIC	SGprob	DGprob	Selected Model
AS2COS0001.1	0.73	0.67	DG	SG	0.49	0.51	DG
AS2COS0002.1	1.53	1.26	DG	DG	0.18	0.82	DG
AS2COS0006.1	1.29	0.91	DG	DG	0.15	0.85	DG
AS2COS0008.1	2.41	1.80	DG	DG	0.13	0.87	DG
AS2COS0009.1	2.27	1.96	DG	DG	0.17	0.83	DG
AS2COS0011.1-C I(1-0)	1.20	1.04	DG	DG	0.16	0.84	DG
AS2COS0011.1-CO(5-4)	2.85	1.73	DG	DG	0.14	0.86	DG
AS2COS0013.1	1.42	1.04	DG	DG	0.10	0.90	DG
AS2COS0014.1	1.51	0.95	DG	DG	0.07	0.93	DG
AS2COS0023.1-CO(4-3)	1.33	1.17	DG	DG	0.27	0.73	SG
AS2COS0023.1-CO(5-4)	1.42	1.40	SG	SG	0.60	0.40	SG
AS2COS0028.1-CO(3-2)	0.96	0.84	DG	SG	0.51	0.49	SG
AS2COS0028.1-CO(4-3)	1.23	1.12	DG	SG	0.47	0.53	SG
AS2COS0031.1-CO(4-3)	4.21	1.81	DG	DG	0.19	0.81	DG
AS2COS0031.1-C I(1-0)	0.81	0.64	DG	DG	0.05	0.95	DG
AS2COS0044.1	1.81	0.91	DG	DG	0.21	0.79	DG
AS2COS0054.1	1.82	1.22	DG	DG	0.11	0.89	DG
AS2COS0065.1	2.47	1.36	DG	DG	0.20	0.80	DG
AS2COS0066.1	1.65	1.37	DG	DG	0.07	0.93	DG
AS2COS0090.1	1.65	1.14	DG	DG	0.14	0.86	DG
AS2COS0139.1	0.97	0.80	DG	DG	0.02	0.98	DG

Note. Here SG and DG are abbreviations for single Gaussian and double Gaussian, respectively. The second and third columns provide the reduced χ^2 values of each fit, and the fourth and fifth columns show the preferred selection based on AICc and BIC, respectively.

Appendix B

Further Comparisons between Photometric and Spectroscopic Redshifts

To gain more insight into the redshift assignment for the single line detected SMGs, we compare the adopted spectroscopic redshifts in Table 1 and the photometric redshifts provided by the two well-tested OIR-based catalogs in the COSMOS field, COSMOS2015 (Laigle et al. 2016) and COSMOS2020 (Weaver et al. 2022). Focusing on the primary SMGs, matches to the two catalogs can be found on 14, where the corresponding matches are not exactly the same, and most are found on SMGs with a single line detection. The corresponding redshifts for the matched SMGs are plotted in Figure B1, except for AS2COS0037.1, where no emission line

is detected. Two versions of the photometric redshifts are provided in the COSMOS2020 catalog, and they are both shown. A few key features are worth noting. First, the overall median in redshift difference is consistent with zero for all three sets of comparisons, suggesting that the redshift distribution discussed in Section 4.2 is not affected by the photometric catalogs adopted for determining redshifts for single-line SMGs. Second, compared to Figure 7, OIR-based photometric redshifts tend to miss or underestimate redshifts for the highest-redshift ($z > 4$) SMGs. This is expected, as they tend to be faint or undetected in OIR images. Finally, AS2COS0009.1 has significantly higher photometric redshifts ($\Delta z \gtrsim 1$) in all three matches, suggesting that this source could be one of those that are expected to have incorrect redshift assignments in Table 1. Note that AS2COS0090.1 cannot be at the photometric redshift

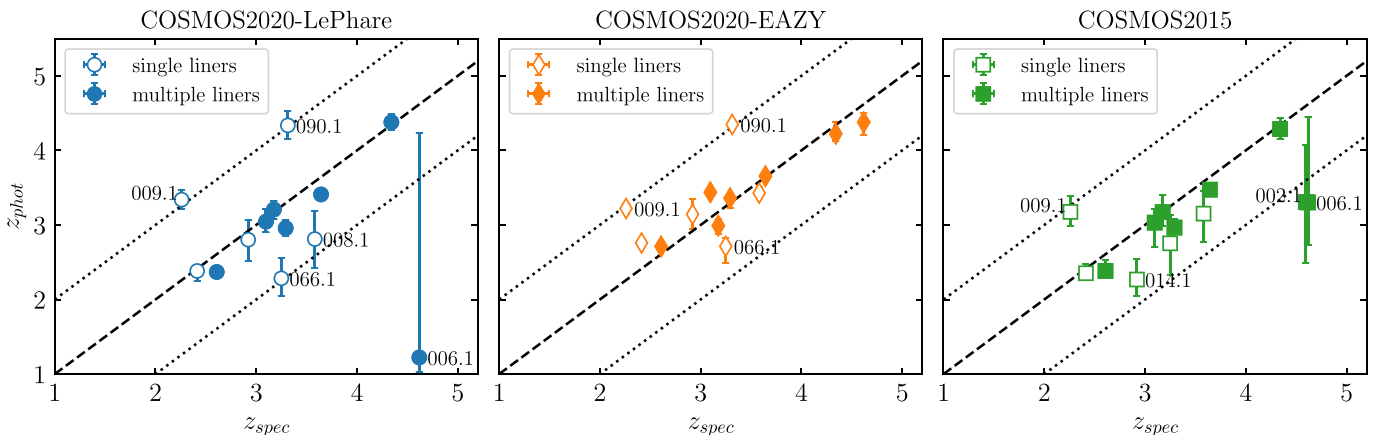


Figure B1. Similar to the top panel of Figure 7, where spectroscopic redshifts are taken from the adopted redshifts in Table 1, and photometric redshifts are based on two COSMOS catalogs, COSMOS2015 (Laigle et al. 2016) and COSMOS2020 (Weaver et al. 2022). Two versions of the redshifts are provided in COSMOS2020, and they are both shown.

deduced from the COSMOS2020 catalog, which is $z \sim 4.3$, as two CO lines would have been detected, like AS2COS0023.1, given the frequency coverage of our data (Figure 5).

ORCID iDs

Chian-Chou Chen (陳建州)  <https://orcid.org/0000-0002-3805-0789>
 Ian Smail  <https://orcid.org/0000-0003-3037-257X>
 A. M. Swinbank  <https://orcid.org/0000-0003-119-5837>
 Y. Ao  <https://orcid.org/0000-0003-3139-2724>
 B. Hatsukade  <https://orcid.org/0000-0001-6469-8725>
 R. J. Ivison  <https://orcid.org/0000-0001-5118-1313>
 Minju M. Lee  <https://orcid.org/0000-0002-2419-3068>
 Stephen Serjeant  <https://orcid.org/0000-0002-0517-7943>
 Hideki Umehata  <https://orcid.org/0000-0003-1937-0573>
 Wei-Hao Wang  <https://orcid.org/0000-0003-2588-1265>
 Y. Zhao  <https://orcid.org/0000-0002-9128-818X>

References

- Alexander, D. M., & Hickox, R. C. 2012, *NewAR*, 56, 93
 An, F. X., Simpson, J. M., Smail, I., et al. 2019, *ApJ*, 886, 48
 Astropy Collaboration, Robitaille, T. P., Tollerud, E. J., et al. 2013, *A&A*, 558, A33
 Bakx, T. J. L. C., Dannerbauer, H., Frayer, D., et al. 2020, *MNRAS*, 496, 2372
 Barger, A. J., Cowie, L. L., Sanders, D. B., et al. 1998, *Natur*, 394, 248
 Barger, A. J., Cowie, L. L., Smail, I., et al. 1999, *AJ*, 117, 2656
 Barger, A. J., Wang, W.-H., Cowie, L. L., et al. 2012, *ApJ*, 761, 89
 Bertin, E., & Arnouts, S. 1996, *A&AS*, 117, 393
 Béthermin, M., Daddi, E., Magdis, G., et al. 2012, *ApJL*, 757, L23
 Béthermin, M., Wu, H.-Y., Lagache, G., et al. 2017, *A&A*, 607, A89
 Binney, J., & Tremaine, S. 2008, *Galactic Dynamics* (2nd ed.; Princeton, NJ: Princeton Univ. Press)
 Birkin, J. E., Weiss, A., Wardlow, J. L., et al. 2021, *MNRAS*, 501, 3926
 Bothwell, M. S., Smail, I., Chapman, S. C., et al. 2013, *MNRAS*, 429, 3047
 Bussmann, R. S., Pérez-Fourmon, I., Amber, S., et al. 2013, *ApJ*, 779, 25
 Bussmann, R. S., Riechers, D., Fialkov, A., et al. 2015, *ApJ*, 812, 43
 Cai, Z.-Y., Lapi, A., Xia, J.-Q., et al. 2013, *ApJ*, 768, 21
 Calistro Rivera, G., Hodge, J. A., Smail, I., et al. 2018, *ApJ*, 863, 56
 Cappellari, M., Scott, N., Alatalo, K., et al. 2013, *MNRAS*, 432, 1709
 Casey, C. M., Cooray, A., Killi, M., et al. 2017, *ApJ*, 840, 101
 Casey, C. M., Narayanan, D., & Cooray, A. 2014, *PhR*, 541, 45
 Casey, C. M., Zavala, J. A., Spilker, J., et al. 2018, *ApJ*, 862, 77
 Chapman, S. C., Blain, A. W., Ivison, R. J., & Smail, I. R. 2003, *Natur*, 422, 695
 Chapman, S. C., Blain, A. W., Smail, I., & Ivison, R. J. 2005, *ApJ*, 622, 772
 Chapman, S. C., Smail, I., Ivison, R. J., & Blain, A. W. 2002, *MNRAS*, 335, L17
 Chen, C.-C., Cowie, L. L., Barger, A. J., et al. 2013, *ApJ*, 776, 131
 Chen, C.-C., Hodge, J. A., Smail, I., et al. 2017, *ApJ*, 846, 108
 Chen, C.-C., Smail, I., Swinbank, A. M., et al. 2015, *ApJ*, 799, 194
 Chen, C.-C., Smail, I., Swinbank, A. M., et al. 2016, *ApJ*, 831, 91
 Cowie, L. L., Barger, A. J., Hsu, L.-Y., et al. 2017, *ApJ*, 837, 139
 Cowie, L. L., González-López, J., Barger, A. J., et al. 2018, *ApJ*, 865, 106
 Cowley, W. I., Lacey, C. G., Baugh, C. M., & Cole, S. 2015, *MNRAS*, 446, 1784
 da Cunha, E., Hodge, J. A., Casey, C. M., et al. 2021, *ApJ*, 919, 30
 da Cunha, E., Walter, F., Smail, I. R., et al. 2015, *ApJ*, 806, 110
 Daddi, E., Rich, R. M., Valentino, F., et al. 2022, *ApJL*, 926, L21
 Danielson, A. L. R., Swinbank, A. M., Smail, I., et al. 2017, *ApJ*, 840, 78
 Davé, R., Anglés-Alcázar, D., Narayanan, D., et al. 2019, *MNRAS*, 486, 2827
 Davidzon, I., Ilbert, O., Laigle, C., et al. 2017, *A&A*, 605, A70
 Davis, T. A., Greene, J. E., Ma, C.-P., et al. 2019, *MNRAS*, 486, 1404
 de Blok, W. J. G., & Walter, F. 2014, *AJ*, 147, 96
 De Breuck, C., Williams, R. J., Swinbank, M., et al. 2014, *A&A*, 565, A59
 Dudzevičiūtė, U., Smail, I., Swinbank, A. M., et al. 2020, *MNRAS*, 494, 3828
 Dye, S., Eales, S. A., Aretxaga, I., et al. 2008, *MNRAS*, 386, 1107
 Dye, S., Eales, S. A., Gomez, H. L., et al. 2022, *MNRAS*, 510, 3734
 Fujimoto, S., Ouchi, M., Kohno, K., et al. 2018, *ApJ*, 861, 7
 Geach, J., Banerji, M., Bertoldi, F., et al. 2019, *BAAS*, 51, 549
 Geach, J. E., Dunlop, J. S., Halpern, M., et al. 2017, *MNRAS*, 465, 1789
 Genzel, R., Price, S. H., Übler, H., et al. 2020, *ApJ*, 902, 98
 Girelli, G., Bolzonella, M., & Cimatti, A. 2019, *A&A*, 632, A80
 González-López, J., Bauer, F. E., Aravena, M., et al. 2017, *A&A*, 608, A138
 González-López, J., Decarli, R., Pavesi, R., et al. 2019, *ApJ*, 882, 139
 Greve, T. R., Bertoldi, F., Smail, I., et al. 2005, *MNRAS*, 359, 1165
 Gullberg, B., Smail, I., Swinbank, A. M., et al. 2019, *MNRAS*, 490, 4956
 Hainline, L. J., Blain, A. W., Smail, I., et al. 2011, *ApJ*, 740, 96
 Hayward, C. C., Behroozi, P. S., Somerville, R. S., et al. 2013a, *MNRAS*, 434, 2572
 Hayward, C. C., Chapman, S. C., Steidel, C. C., et al. 2018, *MNRAS*, 476, 2278
 Hayward, C. C., Narayanan, D., Kereš, D., et al. 2013b, *MNRAS*, 428, 2529
 Hayward, C. C., Sparre, M., Chapman, S. C., et al. 2021, *MNRAS*, 502, 2922
 Hezaveh, Y. D., Marrone, D. P., Fassnacht, C. D., et al. 2013, *ApJ*, 767, 132
 Hickox, R. C., Wardlow, J. L., Smail, I., et al. 2012, *MNRAS*, 421, 284
 Hill, R., Chapman, S. C., Scott, D., et al. 2018, *MNRAS*, 477, 2042
 Hodge, J. A., & da Cunha, E. 2020, *RSOS*, 7, 200556
 Hodge, J. A., Karim, A., Smail, I., et al. 2013, *ApJ*, 768, 91
 Hodge, J. A., Smail, I., Walter, F., et al. 2019, *ApJ*, 876, 130
 Hodge, J. A., Swinbank, A. M., Simpson, J. M., et al. 2016, *ApJ*, 833, 103
 Hughes, D. H., Serjeant, S., Dunlop, J., et al. 1998, *Natur*, 394, 241
 Ikarashi, S., Ivison, R. J., Caputi, K. I., et al. 2015, *ApJ*, 810, 133
 Ilbert, O., McCracken, H. J., Le Fèvre, O., et al. 2013, *A&A*, 556, A55
 Ivison, R. J., Greve, T. R., Dunlop, J. S., et al. 2007, *MNRAS*, 380, 199
 Ivison, R. J., Greve, T. R., Smail, I., et al. 2002, *MNRAS*, 337, 1
 Ivison, R. J., Lewis, A. J. R., Weiss, A., et al. 2016, *ApJ*, 832, 78
 Ivison, R. J., Smail, I., Le Borgne, J.-F., et al. 1998, *MNRAS*, 298, 583
 Jiménez-Andrade, E. F., Zavala, J. A., Magnelli, B., et al. 2020, *ApJ*, 890, 171
 Jones, L. H., Rosenthal, M. J., Barger, A. J., & Cowie, L. L. 2021, *ApJ*, 916, 46
 Jullo, E., & Kneib, J. P. 2009, *MNRAS*, 395, 1319
 Karim, A., Swinbank, A. M., Hodge, J. A., et al. 2013, *MNRAS*, 432, 2
 Kauffmann, G., Heckman, T. M., White, S. D. M., et al. 2003, *MNRAS*, 341, 54
 Kepley, A. A., Tsutsumi, T., Brogan, C. L., et al. 2020, *PASP*, 132, 024505
 Klaassen, P. D., Mroczkowski, T. K., Cicone, C., et al. 2020, *Proc. SPIE*, 11445, 114452F
 Kneib, J., Ellis, R. S., Smail, I., Couch, W. J., & Sharples, R. M. 1996, *ApJ*, 471, 643
 Koprowski, M. P., Dunlop, J. S., Michałowski, M. J., et al. 2016, *MNRAS*, 458, 4321
 Lacey, C. G., Baugh, C. M., Frenk, C. S., et al. 2016, *MNRAS*, 462, 3854
 Lagos, C. d. P., da Cunha, E., Robotham, A. S. G., et al. 2020, *MNRAS*, 499, 1948
 Lagos, C. d. P., Robotham, A. S. G., Trayford, J. W., et al. 2019, *MNRAS*, 489, 4196
 Laigle, C., McCracken, H. J., Ilbert, O., et al. 2016, *ApJS*, 224, 24
 Legrand, L., McCracken, H. J., Davidzon, I., et al. 2019, *MNRAS*, 486, 5468
 Lelli, F., Di Teodoro, E. M., Fraternali, F., et al. 2021, *Sci*, 371, 713
 Lilly, S. J., Eales, S. A., Gear, W. K. P., et al. 1999, *ApJ*, 518, 641
 Lim, C.-F., Chen, C.-C., Smail, I., et al. 2020, *ApJ*, 895, 104
 Limousin, M., Kneib, J.-P., & Natarajan, P. 2005, *MNRAS*, 356, 309
 Litke, K. C., Marrone, D. P., Spilker, J. S., et al. 2019, *ApJ*, 870, 80
 Lovell, C. C., Geach, J. E., Davé, R., Narayanan, D., & Li, Q. 2021, *MNRAS*, 502, 772
 Lovell, M. R., Pillepich, A., Genel, S., et al. 2018, *MNRAS*, 481, 1950
 Manning, S. M., Casey, C. M., Zavala, J. A., et al. 2022, *ApJ*, 925, 23
 McAlpine, S., Smail, I., Bower, R. G., et al. 2019, *MNRAS*, 488, 2440
 McMullin, J. P., Waters, B., Schiebel, D., Young, W., & Golap, K. 2007, in *ASP Conf. Ser. 376, Astronomical Data Analysis Software and Systems XVI*, ed. R. A. Shaw, F. Hill, & D. J. Bell (San Francisco, CA: ASP), 127
 Merlin, E., Fortuni, F., Torelli, M., et al. 2019, *MNRAS*, 490, 3309
 Michałowski, M. J., Dunlop, J. S., Cirasuolo, M., et al. 2012, *A&A*, 541, A85
 Mitsuhashi, I., Matsuda, Y., Smail, I., et al. 2021, *ApJ*, 907, 122
 Muñoz Arancibia, A. M., Navarrete, F. P., Padilla, N. D., et al. 2015, *MNRAS*, 446, 2291
 Narayanan, D., Turk, M. J., Robitaille, T., et al. 2021, *ApJS*, 252, 12
 Navarro, J. F., Frenk, C. S., & White, S. D. M. 1997, *ApJ*, 490, 493
 Negrello, M., Amber, S., Amvrosiadis, A., et al. 2017, *MNRAS*, 465, 3558
 Negrello, M., Hopwood, R., De Zotti, G., et al. 2010, *Sci*, 330, 800
 Negrello, M., Perrotta, F., González-Nuevo, J., et al. 2007, *MNRAS*, 377, 1557
 Neri, R., Cox, P., Omont, A., et al. 2020, *A&A*, 635, A7
 Novak, M., Venemans, B. P., Walter, F., et al. 2020, *ApJ*, 904, 131
 Oteo, I., Zwaan, M. A., Ivison, R. J., Smail, I., & Biggs, A. D. 2016, *ApJ*, 822, 36
 Planck Collaboration, Aghanim, N., Akrami, Y., et al. 2020, *A&A*, 641, A6
 Poppinga, G., Walter, F., Behroozi, P., et al. 2020, *ApJ*, 891, 135
 Reuter, C., Vieira, J. D., Spilker, J. S., et al. 2020, *ApJ*, 902, 78

- Rigopoulou, D., Pereira-Santaella, M., Magdis, G. E., et al. 2018, *MNRAS*, 473, 20
- Rizzo, F., Vegetti, S., Fraternali, F., Stacey, H. R., & Powell, D. 2021, *MNRAS*, 507, 3952
- Safarzadeh, M., Lu, Y., & Hayward, C. C. 2017, *MNRAS*, 472, 2462
- Sanders, D. B., & Mirabel, I. F. 1996, *ARA&A*, 34, 749
- Sanders, D. B., Soifer, B. T., Elias, J. H., et al. 1988, *ApJ*, 325, 74
- Schreiber, C., Glazebrook, K., Nanayakkara, T., et al. 2018, *A&A*, 618, A85
- Simpson, J. M., Smail, I., Dudzevičiūtė, U., et al. 2020, *MNRAS*, 495, 3409
- Simpson, J. M., Smail, I., Swinbank, A. M., et al. 2015a, *ApJ*, 807, 128
- Simpson, J. M., Smail, I., Swinbank, A. M., et al. 2015b, *ApJ*, 799, 81
- Simpson, J. M., Smail, I., Swinbank, A. M., et al. 2019, *ApJ*, 880, 43
- Simpson, J. M., Swinbank, A. M., Smail, I., et al. 2014, *ApJ*, 788, 125
- Smail, I., Ivison, R. J., & Blain, A. W. 1997, *ApJL*, 490, L5
- Smail, I., Ivison, R. J., Owen, F. N., Blain, A. W., & Kneib, J. 2000, *ApJ*, 528, 612
- Spilker, J. S., Marrone, D. P., Aguirre, J. E., et al. 2014, *ApJ*, 785, 149
- Spilker, J. S., Marrone, D. P., Aravena, M., et al. 2016, *ApJ*, 826, 112
- Stach, S. M., Dudzevičiūtė, U., Smail, I., et al. 2019, *MNRAS*, 487, 4648
- Stach, S. M., Smail, I., Amvrosiadis, A., et al. 2021, *MNRAS*, 504, 172
- Stach, S. M., Smail, I., Swinbank, A. M., et al. 2018, *ApJ*, 860, 161
- Stockmann, M., Toft, S., Gallazzi, A., et al. 2020, *ApJ*, 888, 4
- Straatman, C. M. S., Labbé, I., Spitler, L. R., et al. 2014, *ApJL*, 783, L14
- Strandet, M. L., Weiss, A., Vieira, J. D., et al. 2016, *ApJ*, 822, 80
- Swinbank, A. M., Chapman, S. C., Smail, I., et al. 2006, *MNRAS*, 371, 465
- Tacconi, L. J., Genzel, R., Smail, I., et al. 2008, *ApJ*, 680, 246
- Thomas, D., Maraston, C., Schawinski, K., Sarzi, M., & Silk, J. 2010, *MNRAS*, 404, 1775
- Toft, S., Smolčić, V., Magnelli, B., et al. 2014, *ApJ*, 782, 68
- Umehata, H., Tamura, Y., Kohno, K., et al. 2014, *MNRAS*, 440, 3462
- Urquhart, S. A., Bendo, G. J., Serjeant, S., et al. 2022, *MNRAS*, 511, 3017
- Valentino, F., Tanaka, M., Davidzon, I., et al. 2020, *ApJ*, 889, 93
- van der Wel, A., Bezanson, R., D'Eugenio, F., et al. 2021, *ApJS*, 256, 44
- Vieira, J. D., Marrone, D. P., Chapman, S. C., et al. 2013, *Natur*, 495, 344
- Walter, F., Decarli, R., Aravena, M., et al. 2016, *ApJ*, 833, 67
- Wang, W., Cowie, L. L., Barger, A. J., & Williams, J. P. 2011, *ApJL*, 726, L18
- Wardlow, J. L., Cooray, A., De Bernardis, F., et al. 2013, *ApJ*, 762, 59
- Wardlow, J. L., Simpson, J. M., Smail, I., et al. 2018, *MNRAS*, 479, 3879
- Wardlow, J. L., Smail, I., Coppin, K. E. K., et al. 2011, *MNRAS*, 415, 1479
- Weaver, J. R., Kauffmann, O. B., Ilbert, O., et al. 2022, *ApJS*, 258, 11
- Wechsler, R. H., Bullock, J. S., Primack, J. R., Kravtsov, A. V., & Dekel, A. 2002, *ApJ*, 568, 52
- Wilkinson, A., Almaini, O., Chen, C.-C., et al. 2017, *MNRAS*, 464, 1380
- Wu, P.-F., Nelson, D., van der Wel, A., et al. 2021, *AJ*, 162, 201
- Wu, P.-F., van der Wel, A., Gallazzi, A., et al. 2018, *ApJ*, 855, 85
- Zavala, J. A., Casey, C. M., Manning, S. M., et al. 2021, *ApJ*, 909, 165
- Zhang, Z.-Y., Romano, D., Ivison, R. J., Papadopoulos, P. P., & Matteucci, F. 2018, *Natur*, 558, 260